

The OBSIDIAN model: three regimes of black hole feedback

Douglas Rennehan¹, Arif Babul^{2,3}, Belaid Moa⁴ and Romeel Davé^{5,6}

¹Center for Computational Astrophysics, Flatiron Institute, 162 Fifth Avenue, New York, NY 10010, USA

²Department of Physics and Astronomy, University of Victoria, BC V8X 4M6, Canada

³Infosys Visiting Chair Professor, Indian Institute of Science, Bangalore 560012, India

⁴Department of Electrical Engineering/Alliance Canada/WestDRI/University Systems, University of Victoria, BC V8P 5C2, Canada

⁵Institute for Astronomy, University of Edinburgh, Edinburgh EH9 3HJ, UK

⁶Department of Physics and Astronomy, University of the Western Cape, Bellville 7535, South Africa

Accepted 2024 July 22. Received 2024 July 3; in original form 2023 September 29

ABSTRACT

In theoretical models of galaxy evolution, black hole feedback is a necessary ingredient in order to explain the observed exponential decline in number density of massive galaxies. Most contemporary black hole feedback models in cosmological simulations rely on a constant radiative efficiency (usually $\eta \sim 0.1$) at all black hole accretion rates. We present the OBSIDIAN subgrid model, a synthesis model for the spin-dependent radiative efficiencies of three physical accretion rate regimes, i.e. $\eta = \eta(j, \dot{M}_{\text{acc}})$, for use in large-volume cosmological simulations. The three regimes include: an advection-dominated accretion flow ($\dot{M}_{\text{acc}} < 0.03 \dot{M}_{\text{Edd}}$), a quasar-like mode ($0.03 < \dot{M}_{\text{acc}}/\dot{M}_{\text{Edd}} < 0.3$), and a slim disc mode ($\dot{M}_{\text{acc}} > 0.3 \dot{M}_{\text{Edd}}$). Additionally, we include a large-scale powerful jet at low accretion rates. The black hole feedback model we present is a kinetic model that prescribes mass loadings but could be used in thermal models directly using the radiative efficiency. We implement the OBSIDIAN model into the SIMBA galaxy evolution model to determine if it is possible to reproduce galaxy populations successfully, and provide a first calibration for further study. Using a 2×1024^3 particle cosmological simulation in a $(150 \text{ cMpc})^3$ volume, we found that the model is successful in reproducing the galaxy stellar mass function, black hole mass–stellar mass relationship, and stellar mass–halo mass relationship. Moving forward, this model opens new avenues for exploration of the impact of black hole feedback on galactic environments.

Key words: methods: numerical – galaxies: active – galaxies: evolution – galaxies: formation – quasars: supermassive black holes – galaxies: statistics.

1 INTRODUCTION

The details of the physical processes that halt star formation in galaxies (i.e. the *quenching* process) is an open, long-standing question. The foremost candidate to explain the quenching process in galaxies is active galactic nuclei (AGNs) feedback, driven by accretion onto a supermassive black hole (SMBH) (Cattaneo et al. 2009). There is ample observational evidence that every massive galaxy hosts a central SMBH (Kormendy & Ho 2013; Bentz & Manne-Nicholas 2018; Schutte, Reines & Greene 2019; Ding et al. 2020). Combined with the evidence from large-scale galaxy surveys that show AGN-hosting galaxies have significantly lower star formation rates (SFRs) than their non-AGN counterparts (Ellison et al. 2016; Smith et al. 2016; Sanchez et al. 2018; Lacerda et al. 2020; Ellison et al. 2021; Lammers et al. 2023), it is clear that theoretical models of galaxy evolution must include accurate models for the impact of AGN feedback.

SMBHs play an outsized role in galaxy evolution through their extremely efficient conversion of accretion energy into powerful feedback in their environments. That feedback energy must couple

to the gaseous environment in order to prevent star formation. There are two important mechanisms necessary for this to occur. First, AGN feedback is brilliantly on display in the cores of galaxy groups and clusters, in the form of large-scale ($\sim 1 - 10 \text{ kpc}$) jets (Jetha et al. 2008; O’Sullivan et al. 2012; Kuźmicz et al. 2017; Brienza et al. 2023; Chavan, Dabhade & Saikia 2023). These powerful jets ($\sim 50\,000 \text{ km s}^{-1}$) inflate and heat large, radio-emitting bubbles (i.e. the *radio mode* of feedback) in the intracluster medium (Boehringer et al. 1993; Nusser, Silk & Babul 2006; Blanton et al. 2011; Babul, Sharma & Reynolds 2013; Prasad, Sharma & Babul 2015; Cielo et al. 2018; Prasad, Sharma & Babul 2018), which may heat the gas through shocks, sound waves, turbulence, or thermal conduction – preventing gas cooling onto the central galaxy (Reynolds et al. 2005; Conroy & Ostriker 2008; Ruszkowski & Oh 2011; Bourne & Sijacki 2021; Su et al. 2021; Bourne & Yang 2023; Weinberger et al. 2023). Secondly, other galaxies could be more impacted by quasar radiation on the galaxy-scale (i.e. the *quasar mode* of feedback) rather than jets directly (Babul & White 1991; Silk & Rees 1998; King & Pounds 2015). The quasar winds are thought to be launched by radiation pressure on gas close to the SMBH from the accretion process itself (Murray, Quataert & Thompson 2005). They should escape the central region preferentially along the path of least resistance, perpendicular with some opening angle

* E-mail: douglas.rennehan@gmail.com

to the galactic disc with velocities $\sim 1000 \text{ km s}^{-1}$ on $\sim \text{kpc}$ scales (Ciotti, Ostriker & Proga 2009; Faucher-Giguère & Quataert 2012; Fiore et al. 2017). Observations on smaller scales show the existence of ultrafast outflows with velocities up to $\sim 50\,000 \text{ km s}^{-1}$ in the cores of ≈ 20 per cent to 40 per cent of local AGN (Tombesi et al. 2010, 2011; Gofford et al. 2013). Even a small amount of the AGN feedback coupling to the surrounding interstellar or circumgalactic medium should be sufficient to halt star formation in most galaxies.

Save for large-scale collimated jets in galaxy clusters, the accretion and feedback processes within AGN occur on scales close to the SMBH ($\sim 0.1 - 100 \text{ pc}$). Contemporary cosmological simulations with SMBHs have made significant gains in resolution and volume (see e.g. Anglés-Alcázar et al. 2021; Hopkins et al. 2024; Koudmani et al. 2024), however even the most ambitious large-scale simulations achieve effective resolutions on the kpc-scale. Therefore, capturing the complete physics of the AGN while simultaneously simulating thousands of galaxies would require an infeasible increase of a factor of up to $\sim 10^4$ in computation time. For that reason, AGN related physics must be treated with sub-grid scale models – models that approximate the small-scale physics and link to the resolved scale (for excellent reviews see Somerville & Davé 2015; Naab & Ostriker 2017; Crain & van de Voort 2023).

The first subgrid models for AGN feedback in galaxy-scale simulations were highly simplified, but were able to show that merging disc galaxies power an AGN that is able to quench star formation (Di Matteo, Springel & Hernquist 2005; Springel, Di Matteo & Hernquist 2005; Di Matteo et al. 2008). Most contemporary models use a similar approach, where a small, tunable fraction $\epsilon_f \sim 0.05$ of the bolometric luminosity of the AGN couples to medium, providing all of the necessary energy. Typically, the luminosity is parametrized as $L = \eta \dot{M}_{\text{acc}} c^2$, with η being the radiative efficiency and \dot{M}_{acc} the accretion rate onto the black hole (Soltan 1982). Since these models were originally motivated by quasars in post-merger galaxies, the radiative efficiency is usually taken as a constant $\eta \sim 0.1$. Indeed, quasar mode feedback is effective at clearing out the gas in the cores of simulated galaxies, which regulates the SFR in the galaxy, as well as preventing the SMBH from growing too rapidly (Silk & Rees 1998; Sazonov et al. 2005; Cattaneo et al. 2009), explaining the relationship between SMBH mass and central velocity dispersion (Kormendy & Ho 2013). While the quasar mode is effective in lower mass haloes, the radio mode is necessary in massive galaxies (Nemmen et al. 2007) at the galaxy group and cluster scale (Nusser et al. 2006; McCarthy et al. 2008; Cielo et al. 2018; Oppenheimer et al. 2021; Jung et al. 2022).

There are a plethora of inventive ways to actually implement these energetics into cosmological simulations. However, AGN feedback models depend on the resolution, hydrodynamical method, and pure philosophical choice. There have been several large-volume simulations, with volumes greater than $(100 \text{ cMpc})^3$, simulated over the last decade with different AGN feedback models. The original ILLUSTRIS simulation modelled AGN feedback by thermally dumping energy directly in the gas surrounding SMBHs at high accretion rates, while producing radio bubbles directly in the halo gas on large scales (Sijacki et al. 2007; Vogelsberger et al. 2014; Sijacki et al. 2015). In subsequent work, ILLUSTRISNG (The Next Generation) modelled the low accretion rate regime with a kinetic wind rather than radio bubbles (Weinberger et al. 2017; Pillepich et al. 2018). The EAGLE simulations used a similar style of feedback to ILLUSTRIS, where the simulated SMBHs dumped thermal energy locally in the surrounding gas, although with a reservoir that stored energy until it could overcome the artificially high cooling rates in the simulated

interstellar medium (Booth & Schaye 2009; Dalla Vecchia & Schaye 2012; Rosas-Guevara et al. 2015; Schaye et al. 2015). HORIZON-AGN introduced a similar split in accretion rate ratios, where rapidly accreting SMBHs dumped thermal energy directly to the surrounding gas (Dubois et al. 2014; Kaviraj et al. 2017). At low accretion rates, the SMBHs ejected a bipolar jet with a 10 per cent efficiency (Dubois et al. 2012). Contrary to the popular thermal dump, the SIMBA simulations convert the simulated SMBH luminosities to kinetic power, in order to power kinetic winds (Davé et al. 2019). At low accretion rate ratios, they use a powerful kinetic jet that ramps up in power as the SMBH accretion rate drops. Recently, the FLAMINGO simulations reintroduced a model similar to the original EAGLE simulations, but added a kinetic jet with very low efficiency of 1.5 per cent at low accretion rates in some of their non-fiducial tests (Huško et al. 2022; Schaye et al. 2023).

There have been several improvements to AGN feedback models in zoom-in simulations, which focus on high-resolution simulations of individual haloes. For example, SIMBA was recalibrated for THE 300 simulations (Cui et al. 2022), EAGLE recalibrated for the C-EAGLE (Barnes et al. 2017), and BAHAMAS (McCarthy et al. 2017) suites of galaxy clusters, HORIZON-AGN updated to the NEWHORIZON simulation (Dubois et al. 2021), and ILLUSTRIS recalibrated and updated for the FABLE simulations (Henden et al. 2018). Similarly, the ROMULUS suite (Tremmel et al. 2017) and the FIRE suite (Hopkins et al. 2014, 2018, 2023) are focused, high-resolution simulations that include AGN feedback models. In both cases, they use quasar-like feedback although the FIRE simulations have dual mode thermal/kinetic injection of energy into the gas surrounding their simulated SMBHs (Wellons et al. 2023), whereas ROMULUS uses a single thermal dump.

Large-volume cosmological simulations that include AGN feedback have been able to reproduce the downturn in the galaxy stellar luminosity function by dropping the star formation efficiency in massive galaxies, thereby quenching them. While these models are impressive feats, all of the *large-volume* implementations usually model a quasar mode constant radiative efficiency $\eta \sim 0.1$, combined with some radio-mode feedback model at some tunable, low accretion rate. However, the power available to feedback in the environment depends on both the spin of the SMBH and the accretion rate in a more complicated manner than a single threshold, and it is important to revisit this as it is a key parameter in determining the overall physics of the system.

SMBHs are characterized by three parameters: mass M_{BH} , angular momentum J , and charge although they typically have zero charge (Blandford & Znajek 1977). The angular momentum is normally recast into the dimension-less spin, j , of the SMBH via $j = Jc/GM_{\text{BH}}^2$, where c is the speed of light and G is Newton’s gravitational constant. The dimension-less spin is restricted to the range $-1 < j < 1$, and SMBHs may change their angular momentum through mergers with other SMBHs or through accretion (Bardeen & Petterson 1975; Scheuer & Feiler 1996; Gammie, Shapiro & McKinney 2004; Berti & Volonteri 2008; Reynolds et al. 2012; Babul et al. 2013; Ricarte, Narayan & Curd 2023). The geometry of accretion flows is complex, but the standard models usually involve magnetized discs and hot accretion flows at low accretion rates, or combinations thereof. The radiative and jet efficiencies of the accretion process depends on the structure of the discs and, in particular, the innermost, spin-dependent, boundary condition near the SMBH (Bardeen 1970; Thorne 1974; Gammie 1999; Narayan, Igumenshchev & Abramowicz 2003). Although the spin distribution of SMBHs is uncertain, the radiative and jet efficiencies usually increase with the spin of

the SMBH (see e.g. Nemmen et al. 2007; Benson & Babul 2009; Reynolds et al. 2012; Tchekhovskoy, McKinney & Narayan 2012).

There are three accretion disc models, separated on the basis of the accretion rate (or luminosity): (i) the advection-dominated accretion flow (ADAF), (ii) thin disc, and (iii) slim disc models.

The ADAF model describes a system of a geometrically thick, optically thin hot gas that may be combined with a truncated thin disc at some outer radius (a *hot* accretion flow) (Yuan & Narayan 2014). At very low accretion rates ($\dot{M}_{\text{acc}} \lesssim 0.03\dot{M}_{\text{Edd}}$), the flow is hot and unable to cool rapidly causing energy to be advected into the black hole (Esin, McClintock & Narayan 1997). This difference in long cooling times versus short in-fall times leads to the flow to be radiatively inefficient, with η scaling as $\eta \sim \dot{M}_{\text{acc}}/\dot{M}_{\text{Edd}}$. The model has been successful at reproducing the spectral properties of low-luminosity AGNs including the supermassive black hole in the centre of our galaxy. In this regime, it is possible to have a powerful kinetic jet combined with a wind generated from the accretion flow (Benson & Babul 2009).

Accretion flows around black holes which accrete more rapidly ($0.03 \lesssim \dot{M}_{\text{acc}}/\dot{M}_{\text{Edd}} \lesssim 0.3$) are better described by a thin disc model, often modelled as a Shakura-Sunyaev viscous thin disc (Shakura & Sunyaev 1973). In this case, the disc is both geometrically thin and optically thick, as the disc is in local thermal equilibrium and can radiate its viscous heat efficiently (Laor & Netzer 1989). Here the radiative efficiency is the highest, with $\eta \sim 0.1$ for a non-rotating SMBH (Shakura & Sunyaev 1973), although it can be much higher for a rotating SMBH (Bardeen 1970). The model has successfully been used to explain the spectra of quasars which have a notable blackbody feature.

At very high accretion rates ($\dot{M}_{\text{acc}} \gtrsim 0.3\dot{M}_{\text{Edd}}$) the flow becomes optically thick and geometrically thin, but much more optically thick than the thin disc model (Abramowicz et al. 1988; Sądowski et al. 2014). The dissipated energy cannot be radiated rapidly enough and can be advected with the flow leading to a drop in the radiative efficiency ($\eta \sim [\dot{M}_{\text{acc}}/\dot{M}_{\text{Edd}}]^{-1}$) (Sądowski 2009; Madau, Haardt & Dotti 2014; see e.g. Lupi et al. 2016 for an implementation in a cosmological context). The dissipated energy causes a slight thickening of the disc and, therefore, this model has been named the slim disc model (Czerny 2019).

In each of the accretion disc models, the spin impacts the radiative efficiencies directly. The subsequent feedback into the environment of SMBHs is not only dependent on the spin value, but the direction of the spin (Babul et al. 2013; Cenci et al. 2020; Sala et al. 2020). In large-volume cosmological simulations, the resolution is usually too poor to follow the spin-evolution of SMBHs (however, see e.g. Dubois et al. 2021; Schaye et al. 2023). Idealized simulations or cosmological zoom-in simulations provide the ideal test beds for tracking the spin of the SMBH and its impact on the radiative efficiencies and, hence, the SMBH feedback strength (see e.g. Fiacconi, Sijacki & Pringle 2018; Qiu et al. 2019; Talbot, Sijacki & Bourne 2022; Koudmani et al. 2024; Talbot, Sijacki & Bourne 2024). There has been a particular focus on spin and accretion rate dependent radiative efficiencies in the ADAF mode, where the spin dependence can cause spin precession that drives isotropic turbulence and prevent cooling in the cores of galaxy clusters (Beckmann et al. 2019, 2022).

The goal of this work is to incorporate the radiative efficiency scalings (with respect to the accretion rate) from the high-resolution simulations into coarser, large-volume cosmological simulations in a consistent manner. Specifically, we aim to synthesize the disc wind and jet model from Benson & Babul (2009), the slim disc radiative efficiencies from Sądowski et al. (2014), and the standard $\eta \sim 0.1$ quasar-like mode of feedback into a cosmological-scale simulation.

Our goal in this work is not to follow the spin evolution of the SMBHs. This paper is organized as follows. First, in Section 2, we describe the new radiative efficiency model in full mathematical detail along with a kinetic injection mechanism. In Section 3, we describe our motivation for incorporating our model into the SIMBA model, and give details of the implementation. In Section 4, we discuss the calibration of the newly incorporated model. In Section 5, we describe the simulated population of galaxies and broad results. Finally, we summarize our findings in Section 6.

2 PHYSICALLY MOTIVATED BLACK HOLE FEEDBACK

We present a finite state machine for treating SMBH feedback in cosmological simulations. There are three physical regimes which we must consider:

- (i) $\dot{M}_{\text{acc}}/\dot{M}_{\text{Edd}} > R_{\text{upper}}$,
- (ii) $R_{\text{lower}} < \dot{M}_{\text{acc}}/\dot{M}_{\text{Edd}} \leq R_{\text{upper}}$, and
- (iii) $\dot{M}_{\text{acc}}/\dot{M}_{\text{Edd}} \leq R_{\text{lower}}$,

where R_{upper} is the boundary between the slim disc mode and the traditional quasar mode and R_{lower} is the boundary between the ADAF mode and quasar mode. In our notation, the true growth rate of the SMBH is the accretion rate \dot{M}_{acc} accounting for radiative losses,

$$\dot{M}_{\text{BH}} = (1 - \eta(j, \dot{M}_{\text{acc}}))\dot{M}_{\text{acc}}. \quad (1)$$

Note that \dot{M}_{Edd} is the Eddington accretion rate,

$$\dot{M}_{\text{Edd}} \equiv \frac{4\pi G m_p}{\sigma_T \eta_{\text{fixed}} c} M_{\text{BH}}. \quad (2)$$

Here G is Newton's gravitational constant, m_p is the proton mass, σ_T is the Thomson cross-section, c is the speed of light, $\eta_{\text{fixed}} = 0.1$ is a normalization radiative efficiency, and M_{BH} is the mass of the black hole.

We treat each regime as a unique state in which the SMBH exists until the conditions are met to transfer to a new state. The transfer condition is dependent on the current state of the SMBH through the *true accretion rate* onto the SMBH (\dot{M}_{acc}) not the *large-scale mass inflow rate* (\dot{M}_{inflow}). Note that in our model, the transfer between states is instantaneous.

While the boundaries R_{upper} and R_{lower} are only approximate, we fix them to values $R_{\text{upper}} = 0.3$ and $R_{\text{lower}} = 0.03$, in line with theoretical estimates (Laor & Netzer 1989; Maccarone, Gallo & Fender 2003; Greene, Ho & Ulvestad 2006; McClintock et al. 2006; Sądowski 2009; Madau et al. 2014).

In Fig. 1, we show the bolometric luminosity (top) and spin-dependent radiative efficiencies (bottom) that we use throughout this work. In both panels, the solid lines show the values for the non-jet component, whereas the dash-dotted lines show the jet component. The dotted vertical lines show the thresholds between the three regimes of feedback, depending on the accretion rate ratio $\dot{M}_{\text{acc}}/\dot{M}_{\text{Edd}}$. We produced the top panel directly from the bottom via the equation $L = \eta(j, \dot{M}_{\text{acc}})\dot{M}_{\text{acc}}c^2$. The η scalings for the low accretion rate and high accretion rate regime were taken from Benson & Babul (2009) and Madau et al. (2014), respectively, and the normalization was found by ensuring continuity in the radiative efficiency in all regimes (starting with the high accretion rate regime). We discuss the radiative efficiency functions in the following subsections.

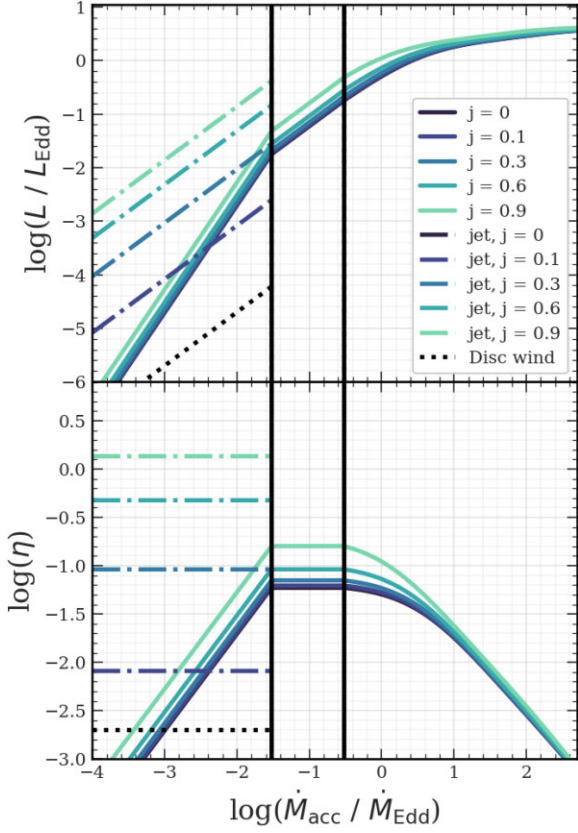


Figure 1. (top) The black hole bolometric luminosity as a function of the small-scale accretion rate. (bottom) The radiative efficiency as a function of the small-scale accretion rate. In both panels, the line colours show the black hole spin, j , increasing from dark to light, respectively. The solid lines show the small scale feedback luminosity and the dash-dotted lines show the jet power. The dashed vertical lines show the boundaries between the three accretion regimes. As black hole spin increases, the black hole draws more power from the accretion flow and the jet becomes significantly more powerful. The typical feedback model uses a radiative efficiency $\eta \sim 0.1$ which corresponds to the middle accretion rate regime.

2.1 Slim disc mode

For the high accretion rate regime we follow Lupi et al. (2016) and use the radiative efficiency from Sądowski et al. (2014), and Madau et al. (2014).

$$\eta_{\text{high}}(j, r) = \frac{r}{16} A(j) \left[\frac{0.985}{r + B(j)} + \frac{0.015}{r + C(j)} \right], \quad (3)$$

where j is the black hole spin parameter and $r \equiv \dot{M}_{\text{Edd}}^* / \dot{M}_{\text{acc}}$. Note $\dot{M}_{\text{Edd}}^* \neq \dot{M}_{\text{Edd}}$; it is defined as $\dot{M}_{\text{Edd}}^* \equiv 16 L_{\text{Edd}} / c^2$ or $\dot{M}_{\text{Edd}}^* = 1.6 \dot{M}_{\text{Edd}}$. Additionally,

$$A(j) \equiv (0.9663 - 0.9292j)^{-0.5639}, \quad (4)$$

$$B(j) \equiv (4.627 - 4.445j)^{-0.5524}, \quad (5)$$

and

$$C(j) \equiv (827.3 - 718.1j)^{-0.7060}. \quad (6)$$

The accretion rate onto the SMBH \dot{M}_{acc} is the difference between the large-scale mass flow rate and the outflowing wind

$$\dot{M}_{\text{acc}} = \dot{M}_{\text{inflow}} - \dot{M}_{\text{wind}} = \dot{M}_{\text{inflow}} - \psi_{\text{slim}}(j, \dot{M}_{\text{acc}}) \dot{M}_{\text{acc}}, \quad (7)$$

where we assume a mass loading of $\psi_{\text{slim}}(j, \dot{M}_{\text{acc}})$ between \dot{M}_{acc} and the wind mass outflow rate, \dot{M}_{wind} (Choi et al. 2012, 2015, 2017). Following the approach in Davé et al. (2019), we assume the SMBH powers a wind via a momentum loading (Murray et al. 2005)

$$\dot{M}_{\text{wind}} v_{\text{wind}} = \frac{20 L_{\text{BH}}}{c} = 20 \eta(j, \dot{M}_{\text{acc}}) \dot{M}_{\text{acc}} c, \quad (8)$$

where \dot{M}_{wind} is the mass outflow rate, v_{wind} is the wind velocity, and $\eta(j, \dot{M}_{\text{acc}})$ is the radiative efficiency. We assume ~ 20 following Faucher-Giguère & Quataert (2012) and Zubovas & King (2012). Therefore,

$$\psi_{\text{slim}}(j, \dot{M}_{\text{acc}}) = \frac{\dot{M}_{\text{wind}}}{\dot{M}_{\text{acc}}} = \epsilon_{f, \text{slim}} \frac{20 \eta(j, \dot{M}_{\text{acc}}) c}{v_{\text{wind}}} \equiv \phi \eta(j, \dot{M}_{\text{acc}}), \quad (9)$$

where we have further defined $\phi \equiv 20 c \epsilon_{f, \text{slim}} / v_{\text{wind}}$ in order to show the explicit dependence on η . We introduce a parameter $\epsilon_{f, \text{slim}}$ to control the momentum flux of the wind since the resolution of our simulations cannot accurately capture the hydrodynamical interaction of the wind with the surrounding gaseous medium. We treat both $\epsilon_{f, \text{slim}}$ and v_{wind} as free parameters and we discuss their calibration in Section 4.

We further define the following accretion rate ratios for \dot{M}_{acc} and \dot{M}_{inflow} :

$$\mathcal{R} \equiv \frac{\dot{M}_{\text{acc}}}{\dot{M}_{\text{Edd}}}, \quad \mathcal{R}' \equiv \frac{\dot{M}_{\text{inflow}}}{\dot{M}_{\text{Edd}}}. \quad (10)$$

Using equation (3) for η , we rewrite equation (7) as,

$$\mathcal{R} + \frac{\phi}{16} A(j) \left[\frac{0.985 \mathcal{R}}{1 + (5/8) B(j) \mathcal{R}} + \frac{0.015 \mathcal{R}}{1 + (5/8) C(j) \mathcal{R}} \right] = \mathcal{R}'. \quad (11)$$

We further simplify this equation by multiplying the entire equation by $[1 + (5/8) B(j) \mathcal{R}][1 + (5/8) C(j) \mathcal{R}] = 1 + (5/8) (B(j) + C(j)) \mathcal{R} + (5/8)^2 B(j) C(j) \mathcal{R}^2$ and reducing to obtain

$$\begin{aligned} & \mathcal{R} + \frac{5}{8} (B(j) + C(j)) \mathcal{R}^2 + \left(\frac{5}{8}\right)^2 B(j) C(j) \mathcal{R}^3 + \\ & \frac{\phi}{16} A(j) \left(\mathcal{R} + \frac{5}{8} [0.015 B(j) + 0.985 C(j)] \mathcal{R}^2 \right) \\ & = \mathcal{R}' + \frac{5}{8} (B(j) + C(j)) \mathcal{R} \mathcal{R}' + \left(\frac{5}{8}\right)^2 B(j) C(j) \mathcal{R}^2 \mathcal{R}'. \end{aligned} \quad (12)$$

This is a cubic equation in \mathcal{R} (i.e. $\dot{M}_{\text{acc}} / \dot{M}_{\text{Edd}}$) since we know $B(j)$, $C(j)$, \dot{M}_{Edd} , and \mathcal{R}' (i.e. $\dot{M}_{\text{inflow}} / \dot{M}_{\text{Edd}}$) at simulation time. Reducing the equation,

$$f(\mathcal{R}) = \alpha_3 \mathcal{R}^3 + \alpha_2 \mathcal{R}^2 + \alpha_1 \mathcal{R} + \alpha_0 = 0, \quad (13)$$

where we have defined

$$\begin{aligned} \alpha_3 & \equiv \left(\frac{5}{8}\right)^2 B(j) C(j), \\ \alpha_2 & \equiv \frac{5}{8} \left[B(j) + C(j) + \frac{\phi}{16} A(j) (0.015 B(j) \right. \\ & \quad \left. + 0.985 C(j)) - \frac{5}{8} B(j) C(j) \mathcal{R}' \right], \\ \alpha_1 & \equiv 1 + \frac{\phi}{16} A(j) - \frac{5}{8} (B(j) + C(j)) \mathcal{R}', \text{ and} \\ \alpha_0 & \equiv -\mathcal{R}'. \end{aligned} \quad (14)$$

In the top panel of Fig. 2, we show the function $f(\mathcal{R})$ from equation (13) for values of j , ϕ , and \mathcal{R}' . The lines show spin values $j \in \{0, 0.3, 0.6, 0.9, 0.9999\}$ from darkest to lightest, respectively,

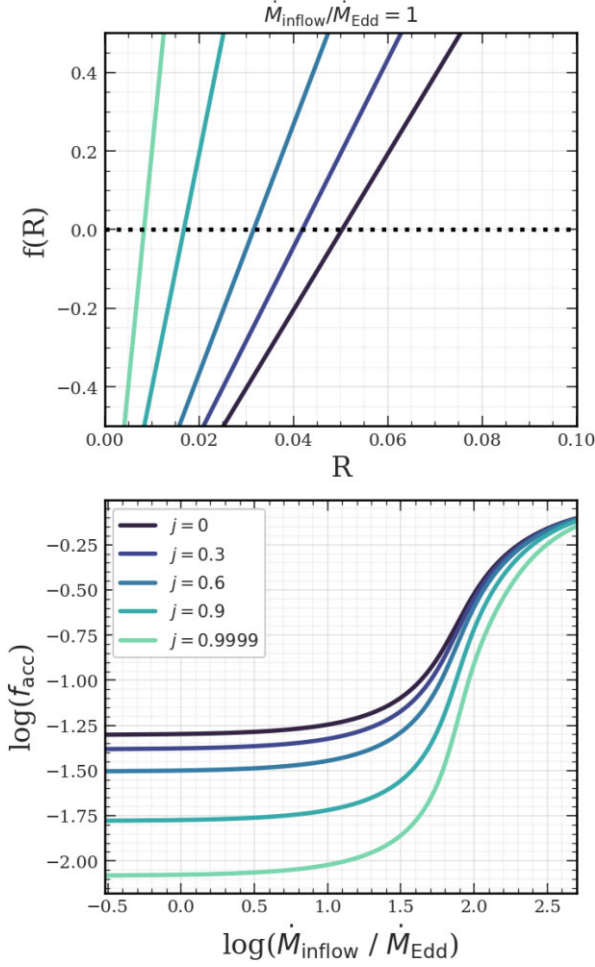


Figure 2. (top) Examples of the cubic function $f(\mathcal{R})$ for the slim disc mode in equation (13), with fixed $\dot{M}_{\text{inflow}}/\dot{M}_{\text{Edd}} = 1$. The horizontal dashed line shows the zero point of the function, where we solve the cubic equation for $\mathcal{R} \equiv \dot{M}_{\text{acc}}/\dot{M}_{\text{Edd}}$, giving the true accretion rate onto the black hole. (bottom) The accretion fraction, i.e. $f_{\text{acc}} \equiv \dot{M}_{\text{acc}}/\dot{M}_{\text{inflow}}$, for the slim disc mode as a function of the large-scale inflow rate $\dot{M}_{\text{inflow}}/\dot{M}_{\text{Edd}}$. In both panels, the coloured lines show different choices for the black hole spin for low spins (dark) to high spins (light). Higher values of j lead to lower accretion fractions, implying that the black hole has more mass in outflows while simultaneously being more likely to switch from the slim disc mode to the quasar mode (i.e. once $\mathcal{R} = \dot{M}_{\text{acc}}/\dot{M}_{\text{Edd}} < 0.3$).

and we fix $\dot{M}_{\text{inflow}}/\dot{M}_{\text{Edd}} = 1$ as well as ϕ using values $v_{\text{wind}} = 1000 \text{ km s}^{-1}$ and $\epsilon_{\text{f,slim}} = 1$. The dashed line shows $f(\mathcal{R}) = 0$, and the solution for the accretion rate \mathcal{R} lies at the intersection of the solid lines and the dashed line. For this illustrative purpose (a black hole with spin j accreting at the Eddington limit), the predicted true accretion rate \dot{M}_{acc} is much less than the large-scale inflow rate \dot{M}_{inflow} , indicating that a large fraction of \dot{M}_{inflow} is lost in the form of an outflowing wind. In this case, the black hole would not remain in the slim disc mode, and would transition to a new state.

The general behaviour in the slim disc regime is a drop off in radiative efficiency as $\eta \sim (\dot{M}_{\text{acc}}/\dot{M}_{\text{Edd}})^{-1}$ (recall Fig. 1). Our model includes a radiatively driven wind, with only a fraction of \dot{M}_{inflow} entering the SMBH at a rate \dot{M}_{acc} ,

$$\dot{M}_{\text{acc}} = \left(\frac{1}{1 + \psi_{\text{slim}}(j, \dot{M}_{\text{acc}})} \right) \dot{M}_{\text{inflow}}. \quad (15)$$

Accounting for the radiative losses, the true mass growth rate of the BH is given by

$$\dot{M}_{\text{BH}} = \left(\frac{1 - \eta(j, \dot{M}_{\text{acc}})}{1 + \psi_{\text{slim}}(j, \dot{M}_{\text{acc}})} \right) \dot{M}_{\text{inflow}}. \quad (16)$$

The bottom panel of Fig. 2 shows the behaviour of $f_{\text{acc}} \equiv \dot{M}_{\text{acc}}/\dot{M}_{\text{inflow}}$ as a function of the large-scale accretion rate $\dot{M}_{\text{inflow}}/\dot{M}_{\text{Edd}}$. The lines are coloured by the spin j , just as the top panel. There is a factor of ~ 100 difference in the accretion fractions depending on the large-scale inflow rate, indicating that, at the highest inflow rates ($\dot{M}_{\text{inflow}}/\dot{M}_{\text{Edd}} \gtrsim 10^2$), the black holes should be able to grow very rapidly due to a lack of a radiatively driven outflowing wind. Note that this behaviour depends on v_{wind} and $\epsilon_{\text{f,slim}}$ and, therefore, these parameters directly control the growth speed of the black holes in this regime.

2.2 Quasar mode

We treat the energetics in the quasar mode identically as in the slim disc mode, except with a radiative efficiency that only depends on the spin of the black hole, $\eta = \eta(j)$. To reiterate, the accretion rate onto the SMBH is the difference between the large-scale inflow rate and the mass outflow rate,

$$\dot{M}_{\text{acc}} = \dot{M}_{\text{inflow}} - \dot{M}_{\text{wind}} = \dot{M}_{\text{inflow}} - \psi_{\text{quasar}}(j) \dot{M}_{\text{acc}}. \quad (17)$$

Therefore, we have

$$\dot{M}_{\text{acc}} = \frac{1}{1 + \psi_{\text{quasar}}(j)} \dot{M}_{\text{inflow}}. \quad (18)$$

Now, we assume that the radiative wind carries a momentum $\sim 20L_{\text{BH}}/c$

$$\dot{M}_{\text{wind}} v_{\text{wind}} = \epsilon_{\text{f,quasar}} \left(\frac{20L_{\text{BH}}}{c} \right) = \epsilon_{\text{f,quasar}} [20\eta(j) \dot{M}_{\text{acc}} c], \quad (19)$$

where $\eta(j)$ is the radiative efficiency and, like $\epsilon_{\text{f,slim}}$, $\epsilon_{\text{f,quasar}}$ is a free parameter that describes the fraction of $20L/c$ that should be used in the simulation to account for resolution effects.

With these results, the energy, momentum, and mass fluxes in the wind are given by

$$\dot{E}_{\text{wind}} = \frac{200(\epsilon_{\text{f,quasar}} \eta(j))^2}{\psi_{\text{quasar}}(j)(1 + \psi_{\text{quasar}}(j))} \dot{M}_{\text{inflow}} c^2, \quad (20)$$

$$\dot{p}_{\text{wind}} = \frac{20\epsilon_{\text{f,quasar}} \eta(j)}{1 + \psi_{\text{quasar}}(j)} \dot{M}_{\text{inflow}} c, \quad (21)$$

and

$$\dot{M}_{\text{wind}} = \frac{\psi_{\text{quasar}}(j)}{1 + \psi_{\text{quasar}}(j)} \dot{M}_{\text{inflow}}, \quad (22)$$

respectively. Accounting for radiative losses, the true mass growth rate of the black hole is

$$\dot{M}_{\text{BH}} = [1 - \eta(j)] \dot{M}_{\text{acc}} = \frac{1 - \eta(j)}{1 + \psi_{\text{quasar}}(j)} \dot{M}_{\text{inflow}}. \quad (23)$$

2.3 Advection-dominated accretion flow mode

At the lowest accretion rates, we model both an isotropic feedback component and a jet emanating from the region surrounding the SMBH. For the isotropic component, we assume that it is powered by outflows engendered by magnetic fields in the rotating flow near the SMBH, i.e. a *disc* wind with efficiency η_{disc} . For the disc wind power, Benson & Babul (2009) suggest a constant value of $\eta_{\text{disc}} \sim 0.002$.

We model the jet component via the Blandford & Znajek (1977) mechanism, where twisted magnetic field lines can extract energy from a rotating SMBH. The increase in magnetic pressure provides the mechanism to launch the jet, and we follow Talbot, Bourne & Sijacki (2021) by using their Blandford-Znajek efficiency,

$$\eta_{\text{jet}}(j) = \frac{\kappa}{4\pi} \phi_{\text{BH}}^2(j) f(j), \quad (24)$$

where $\kappa = 1/(6\pi)$, ϕ_{BH} is the dimension-less magnetic flux, and $f(j)$ is some function of the SMBH spin. For ϕ_{BH} , we follow Huško et al. (2022) and use the results for the spin-dependent magnetic flux from Narayanan et al. (2021),

$$\phi_{\text{BH}}(j) = -20.2j^3 - 14.9j^2 + 34j + 52.6. \quad (25)$$

For $f(j)$, we use the result in Talbot et al. (2021) from Tchekhovskoy et al. (2012),

$$f(j) = \mathcal{J}^2(j) + 1.38\mathcal{J}^4(j) - 9.2\mathcal{J}^6(j), \quad (26)$$

where

$$\mathcal{J} \equiv \frac{j}{2(1 + \sqrt{1 - j^2})}. \quad (27)$$

To model these processes, we first consider mass conservation. Not all of \dot{M}_{inflow} reaches the SMBH, as some of that material is outflowing as a jet or converted into energy. That is represented by the mass balance

$$\dot{M}_{\text{acc}} = \dot{M}_{\text{inflow}} - \dot{M}_{\text{jet}} - \dot{M}_{\text{wind}}, \quad (28)$$

where \dot{M}_{jet} is the mass outflow rate of the jet and \dot{M}_{wind} is the mass outflow rate of the isotropic component. In both cases we assume there is a mass loading rate such that

$$\dot{M}_{\text{acc}} = \dot{M}_{\text{inflow}} - \psi_{\text{jet}}(j)\dot{M}_{\text{acc}} - \psi_{\text{ADAF}}\dot{M}_{\text{acc}} \quad (29)$$

and, therefore,

$$\dot{M}_{\text{acc}} = \frac{1}{1 + \psi_{\text{jet}}(j) + \psi_{\text{ADAF}}} \dot{M}_{\text{inflow}}. \quad (30)$$

The true growth rate of the SMBH must account for radiative losses, as well as the rest-mass energy extracted to power the jet

$$\dot{M}_{\text{BH}} = \dot{M}_{\text{acc}} - \frac{L_{\text{rad}}}{c^2} - \frac{\dot{E}_{\text{jet}}}{c^2}, \quad (31)$$

where $L_{\text{rad}} = \eta(j, \dot{M}_{\text{acc}})\dot{M}_{\text{acc}}c^2$, $\dot{E}_{\text{jet}} = \eta_{\text{jet}}(j)\dot{M}_{\text{acc}}c^2$, and c is the speed of light. Here, $\eta(j, \dot{M}_{\text{acc}}) \propto \dot{M}_{\text{acc}}/\dot{M}_{\text{Edd}}$ and we obtain the jet efficiency η_{jet} from equation (23) in Talbot et al. (2021). We substitute these relations into equation (31) to obtain the true accretion rate onto the SMBH in terms of \dot{M}_{acc} ,

$$\dot{M}_{\text{BH}} = [1 - \eta(j, \dot{M}_{\text{acc}}) - \eta_{\text{jet}}(j)]\dot{M}_{\text{acc}}. \quad (32)$$

Equation (30) allows us to link \dot{M}_{acc} to the large-scale inflow rate, \dot{M}_{inflow} . First, to obtain our final equation, we must ensure continuity in η across all states by scaling the radiative efficiency to the value at R_{lower} ,

$$\eta(j, \dot{M}_{\text{acc}}) = \eta(j, R_{\text{lower}}) \left(\frac{\dot{M}_{\text{acc}}}{\dot{M}_{\text{Edd}}} \right). \quad (33)$$

This is valid for $\dot{M}_{\text{acc}}/\dot{M}_{\text{Edd}} < R_{\text{lower}}$. Finally, combining equations (30), (32), and (33) gives the final true SMBH growth rate in terms of \dot{M}_{inflow} ,

$$\dot{M}_{\text{BH}} = \left[\frac{1 - \frac{\eta(j, R_{\text{lower}})\dot{M}_{\text{inflow}}}{(1 + \psi_{\text{jet}}(j) + \psi_{\text{ADAF}})\dot{M}_{\text{Edd}}} - \eta_{\text{jet}}(j)}{1 + \psi_{\text{jet}}(j) + \psi_{\text{ADAF}}} \right] \dot{M}_{\text{inflow}}. \quad (34)$$

All that remains is to determine both $\psi_{\text{jet}}(j)$ and ψ_{ADAF} . However, there are a few important considerations before we may determine the mass loadings for the jet and isotropic wind.

For the jet, one could assume that it conserves either the launch momentum or the launch energy. On small scales, we expect the jet to approximately conserve energy as it is injected very close to the SMBH. However, the scales of simulations in this work are much larger than the inner accretion flow. By the time the jet reaches our resolution in the intracluster medium (approx. 10 kpc), we would expect that material has been swept up in a larger flow, loaded with momentum. Indeed, observational techniques to determine the velocities of jets on large-scales show that the advance velocities are $\sim 5000\text{--}10\,000 \text{ km s}^{-1}$ (Jamrozy et al. 2005; Machalski et al. 2007) which is much slower than a typical, expected launch velocity of $50\,000 \text{ km s}^{-1}$ (see e.g. Tombesi et al. 2011, 2014; Morganti 2017). We experimented with energy conservation and found that only a narrow range of v_{jet} was possible and, therefore, we choose to model both a small-scale energy loading $\psi_{\text{jet}}(j)$ combined with a resolved momentum loading $\psi_{\text{jet, res}}(j)$.

It is important to emphasize that $\psi_{\text{jet}}(j)$ enters directly into the mass balance through equations (30) and (34). Consider the case when $\psi_{\text{ADAF}} \rightarrow 0$, then the accretion fraction of \dot{M}_{inflow} to \dot{M}_{BH} is,

$$f_{\text{acc}} = \frac{1 - \eta_{\text{jet}}(j)}{1 + \psi_{\text{jet}}(j)}. \quad (35)$$

In the case that $\eta_{\text{jet}} > 1$, the jet should be extracting rotational energy from the SMBH thereby reducing the overall mass – which is the irreducible mass combined with the rotational energy (i.e. E/c^2). Since we do not model the spin-up or spin-down of the SMBH, we also do not subtract η_{jet} from the accretion fraction to avoid negative SMBH masses in the simulation. Additionally, $\psi_{\text{jet}}(j)$ is degenerate with the accretion rate normalization. For that reason, we fix the small-scale mass loading factor to $\psi_{\text{jet}}(j) = 2000$ at $\eta_{\text{jet}}(j) = 1$ such that the SMBHs remain on the BH mass–stellar mass relationship.

To compute the resolved mass loading, $\psi_{\text{jet, res}}(j)$, we use a momentum constraint assuming that the jet is electromagnetic in origin,

$$\dot{P}_{\text{jet}} = \frac{\dot{E}_{\text{jet}}}{c} = \eta_{\text{jet}}(j)\dot{M}_{\text{acc}}c = \dot{M}_{\text{jet}}v_{\text{jet}}, \quad (36)$$

where v_{jet} is the jet velocity, and $\eta_{\text{jet}}(j)$ is the jet energy efficiency. Rearranging, we find $\psi_{\text{jet, res}}(j)$ in terms of the free parameter v_{jet} ,

$$\psi_{\text{jet, res}}(j) \equiv \eta_{\text{jet}}(j) \left(\frac{c}{v_{\text{jet}}} \right). \quad (37)$$

The sub-grid jet energy and momentum are

$$\dot{E}_{\text{jet, sub}} = \frac{\eta_{\text{jet}}}{1 + \psi_{\text{jet}}(j) + \psi_{\text{ADAF}}} \dot{M}_{\text{inflow}}c^2, \quad (38)$$

and

$$\dot{P}_{\text{jet, sub}} = \frac{\eta_{\text{jet}}}{1 + \psi_{\text{jet}}(j) + \psi_{\text{ADAF}}} \dot{M}_{\text{inflow}}c, \quad (39)$$

respectively. Given the momentum constraint, the resolved energy, momentum, and mass fluxes in the jet follow immediately as,

$$\dot{E}_{\text{jet}} = \frac{1}{2} \frac{\psi_{\text{jet, res}}(j)}{1 + \psi_{\text{jet}}(j) + \psi_{\text{ADAF}}} \dot{M}_{\text{inflow}}v_{\text{jet}}^2 \quad (40)$$

$$\dot{P}_{\text{jet}} = \frac{\psi_{\text{jet, res}}(j)}{1 + \psi_{\text{jet}}(j) + \psi_{\text{ADAF}}} \dot{M}_{\text{inflow}}v_{\text{jet}}, \quad (41)$$

and,

$$\dot{M}_{\text{jet}} = \frac{\psi_{\text{jet, res}}(j)}{1 + \psi_{\text{jet}}(j) + \psi_{\text{ADAF}}} \dot{M}_{\text{inflow}}, \quad (42)$$

Table 1. In all of our cosmological simulations we use a cosmology consistent with the observed parameters from the Planck Collaboration XIII 2015.

Parameter	Value
Ω_m	0.3
Ω_Λ	0.7
Ω_b	0.048
h	0.68
σ_8	0.82
n_s	0.97

respectively. Our model assumes that $\dot{P}_{\text{jet,sub}} = \dot{P}_{\text{jet}}$, leading to energy losses in the jet that scale with the resolved jet velocity

$$\frac{\dot{E}_{\text{jet}}}{\dot{E}_{\text{jet,sub}}} = \frac{1}{2} \frac{v_{\text{jet}}}{c}. \quad (43)$$

To compute ψ_{ADAF} , we assume that the hot ADAF outflows are energy conserving,

$$\frac{1}{2} \dot{M}_{\text{wind}} v_{\text{wind}}^2 = \epsilon_{\text{f,ADAF}} \eta_{\text{disc}} \dot{M}_{\text{acc}} c^2, \quad (44)$$

where $\epsilon_{\text{f,ADAF}}$ is a free parameter that describes the coupling of the energy to the wind, and v_{wind} is the wind velocity free parameter. Rearranging gives us an equation for ψ_{ADAF} ,

$$\psi_{\text{ADAF}} \equiv 2\epsilon_{\text{f,ADAF}} \eta_{\text{disc}} \left(\frac{c}{v_{\text{wind}}} \right)^2. \quad (45)$$

Similar to the jet, the energy, momentum, and mass rates are fully specified as,

$$\dot{E}_{\text{wind}} = \frac{\epsilon_{\text{f,ADAF}} \eta_{\text{disc}}}{1 + \psi_{\text{jet}}(j) + \psi_{\text{ADAF}}} \dot{M}_{\text{inflow}} c^2, \quad (46)$$

$$\dot{P}_{\text{wind}} = \frac{\sqrt{2}\epsilon_{\text{f,ADAF}} \eta_{\text{disc}} \psi_{\text{ADAF}}}{1 + \psi_{\text{jet}}(j) + \psi_{\text{ADAF}}} \dot{M}_{\text{inflow}} c, \quad (47)$$

and,

$$\dot{M}_{\text{wind}} = \frac{\psi_{\text{ADAF}}}{1 + \psi_{\text{jet}}(j) + \psi_{\text{ADAF}}} \dot{M}_{\text{inflow}}, \quad (48)$$

respectively.

3 SIMULATION METHODOLOGY

To test our new black hole feedback model, we use the SIMBA subgrid galaxy formation model as a base (Davé et al. 2019). SIMBA has models for cooling, star formation, stellar feedback, and dust evolution that have been shown to well-reproduce observations of galaxy populations. The model exists in the GIZMO code (Hopkins 2015) which uses the Lagrangian mesh-free finite mass method (Lanson & Vila 2008a, b; Gaburov & Nitadori 2011).

In the following subsections, we discuss the relevant black hole subgrid models adapted from SIMBA that we use in our study. For more details on the cooling, star formation, stellar feedback, and dust models, we refer the reader to Davé et al. (2019). In all of our simulations throughout this study, we use the same cosmological parameters as Davé et al. (2019), which we show in Table 1.

3.1 Seeding

In the SIMBA model, black holes of mass $10^4 M_\odot h^{-1}$ are seeded into galaxies once they become resolved at ~ 100 particles. That mass corresponds to $M_{\text{galaxy}} = 3 \times 10^9 M_\odot$. One behaviour of the

SIMBA model is that black holes typically grow rapidly to the black hole stellar mass relationship, and then grow along that relationship as cold gas removed by the quasar mode feedback balances the accretion rate.

3.2 Accretion and feedback

We model the movement of gas into the environment of the SMBHs via a Bondi accretion estimator combined with an estimator based on the cold gas available within the black hole neighbourhood (\dot{M}_{cold}),

$$\dot{M}_{\text{inflow}} = \dot{M}_{\text{Bondi}} + \dot{M}_{\text{cold}}. \quad (49)$$

To separate the two phases of gas, we use a temperature cut of $T = 10^5 \text{K}$ where we only consider $T > 10^5 \text{K}$ for the Bondi accretion calculations. If gas is at temperatures $T < 10^5 \text{K}$ and is sufficiently dense to be considered star forming ($n_{\text{H}} > 0.13 \text{cm}^{-3}$), we use that gas in the calculation for \dot{M}_{cold} .

For Bondi accretion, we use the usual formulation

$$\dot{M}_{\text{Bondi}} = \frac{4\pi G^2 M_{\text{BH}}^2 \rho_{\text{gas}}}{(c_s^2 + v_{\text{BH}}^2)^{3/2}}, \quad (50)$$

where M_{BH} is the mass of the SMBH, ρ_{gas} is the surrounding hot gas density, c_s is the hot gas sound speed, and v_{BH} is the relative velocity of the SMBH with respect to the surrounding hot gas.

For cold gas accretion, we follow Qiu et al. (2019) and use

$$\dot{M}_{\text{cold}} = \epsilon_{\text{cold}} \frac{M_{\text{cold}}}{t_{\text{ff}}}, \quad (51)$$

where M_{cold} is the cold gas mass surrounding the black hole, $t_{\text{ff}} = (3\pi/32G\rho)^{1/2}$ is the free fall time, and ϵ_{cold} is a free parameter describing the efficiency of accretion. We sum all of the mass within the neighbourhood of the black hole to compute ρ in the free fall time.

Our black hole model for the radiative efficiencies is added directly into the SIMBA model, with modifications to the wind and jet mass loadings, and temperature of the jet. For more details on the numerical implementation of the SIMBA model, see Davé et al. (2019). We briefly describe the original model and modifications below. Note that everything we discuss in this section regarding our quasar mode and slim disc mode are equivalent, since our numerical implementation is identical except for the mass loadings.

First, for the quasar mode, SIMBA uses the implementation of Choi et al. (2012) that assumes some fraction f_{acc} of the inflowing material \dot{M}_{inflow} is driven out as a wind with mass rate \dot{M}_{wind} . That fraction is the same fraction that we use in equation (18),

$$f_{\text{acc}} = \frac{1}{1 + \psi}, \quad (52)$$

where $\psi = \dot{M}_{\text{wind}}/\dot{M}_{\text{inflow}}$ is the mass loading any of the modes we described in the previous section. At a given time-step Δt , we compute the accretion rate using equation (49) and subsequently the total mass that should be accreted in that step as

$$M_{\text{acc}} = f_{\text{acc}} \dot{M}_{\text{inflow}} \Delta t. \quad (53)$$

Recall that SIMBA has two separate masses for the black hole (BH) particles: a dynamical ($M_{\text{BH,dyn}}$) and a subgrid mass ($M_{\text{BH,sub}}$). The physical mass represents the dynamical mass for the gravity calculations, and the subgrid mass represents the true, physical mass of the BH on subgrid scales. The separation between the masses is necessary since our particle mass resolution is much coarser than the seed mass. If the dynamical mass were equal to the seed mass, then the dynamics of the simulated BHs would be noisy, leading to BHs

possibly being ejected from the cores of galaxies. At each time-step, we advance $M_{\text{BH,sub}}$ using the accretion rate estimator,

$$(M_{\text{BH,sub}})_{k+1} = (M_{\text{BH,sub}})_k + M_{\text{acc}}, \quad (54)$$

where $(M_{\text{BH,sub}})_k$ is the subgrid BH mass at time-step k .

In the case that $M_{\text{BH,sub}} > M_{\text{BH,dyn}}$, the physical mass has exceeded the dynamical mass and we must extract mass from surrounding particles into the BH to conserve mass. First, we loop over all gas particles within the kernel and compute a probability for accretion,

$$p_i = (M_{\text{BH,sub}} - [M_{\text{BH,dyn}} + M_{\text{acc},j}]) \frac{W_{ij}}{f_{\text{acc}} \rho_{\text{gas}}}, \quad (55)$$

where p_i is the probability of accreting mass from particle i , $M_{\text{acc},j}$ is the cumulative mass counted for accretion in this loop for BH j , W_{ij} is the kernel weight between i and j , and ρ_{gas} is the gas density surrounding BH j . As $(M_{\text{BH,dyn}} + M_{\text{acc},j}) \rightarrow M_{\text{BH,sub}}$, $p_i \rightarrow 0$, ensuring that no further mass is accreted. We boost the probability by f_{acc} to account for feedback, as we only accrete $f_{\text{acc}} M_{\text{gas,part}}$ from each gas particle, and the remainder we drive as a wind. Here $M_{\text{gas,part}}$ is the mass of a gas particle in our simulation. At each time-step, we generate a uniformly distributed random number in the interval $w_i \in [0, 1)$ and only accrete (or select to drive as a wind) from particles with $p_i < w_i$.

It is important to note that mass is automatically conserved when we only accrete f_{acc} of each gas particle, as we boosted our probability by $1/f_{\text{acc}}$. Recall that the accretion fraction corresponds to $1/(1 + \psi)$ and the outflow fraction $\psi/(1 + \psi)$, respectively.

In the case when $M_{\text{BH,sub}} < M_{\text{BH,dyn}}$, mass conservation is not necessary as the total mass accreted has not reached the resolution of the simulation. Therefore, we only have to ensure that feedback processes are resolved,

$$p_i = ([1 - f_{\text{acc}}] \dot{M}_{\text{inflow}}) \Delta t \left(\frac{W_{ij}}{\rho_{\text{gas}}} \right), \quad (56)$$

where $(1 - f_{\text{acc}}) \dot{M}_{\text{inflow}} = \dot{M}_{\text{wind}}$.

Particles selected for accretion are also selected for feedback. Once a particle is selected, we subtract the necessary mass directly from the simulation particle mass. Note that in each BH time-step, we ensure that radiation is accounted for by subtracting off the radiative efficiencies (recall equations 16, 23, and 32). Then, we launch the remaining mass at some velocity v_{wind} or v_{jet} , depending on the mode of feedback. We identify these particles as *wind particles* and, following Davé et al. (2019), decouple them from the hydrodynamics solver and only allow them to feel the effects of gravity. They are decoupled for only a short period of time, and then they fully recouple to the medium. In all cases, we decouple the wind particles for $10^{-4} t_{\text{H}}(z)$, where $t_{\text{H}}(z)$ is the Hubble time at a redshift z . For the quasar and slim disc mode, we choose the local angular momentum direction of the gas within the kernel, \hat{L} , to kick the particles,

$$(\mathbf{v}_{\text{gas,part}})_{k+1} = (\mathbf{v}_{\text{gas,part}})_k \pm v_{\text{wind}} \hat{L}, \quad (57)$$

where $(\mathbf{v}_{\text{gas,part}})_k$ is the gas particle velocity at time-step k . There is a 50 per cent chance of alignment or anti-alignment with \hat{L} . The jet follows the same procedure, except we also heat the gas particles before launch to $T = 10^8$ K and in some calibrations choose a randomly selected isotropic direction.

3.3 Dynamics

Physically, a SMBH moving through a gravitational field experiences a friction force due to its own gravitational wake. The dynamical friction causes SMBHs to lose energy in their orbits and slowly sink

to the centre of their host galaxies. In cosmological simulations, the gravitational resolution is often at the \sim kpc scale and, therefore, dynamical friction is unresolved.¹ For that reason, we assume that SMBHs that form in our simulations are pinned in the centre of their galaxy. Specifically, at each time-step we check each galaxy for its most massive black hole and move it directly to the most bound star particle in the galaxy to ensure it does not escape due to numerical effects.

3.4 Galaxy and halo finding

In all of our cosmological simulations throughout this work we need information about galaxies and their host dark matter haloes. We use the CAESAR package² that uses a friends-of-friends algorithm to find galaxies via groups of cold gas and stars. It also uses this algorithm to find dark matter haloes, and then links the two together into a single galaxy–host relationship.

4 CALIBRATION

Our aim is to provide a more physically motivated model for black hole feedback in cosmological simulations. For that reason, we calibrate our model parameters in cosmological simulations that contain thousands of galaxies. We choose a box size of $L = 25 \text{ cMpc } h^{-1}$ with $N_{\text{gas}} = 256^3$ and $N_{\text{dark}} = 256^3$. This gives a mass resolution of $M_{\text{gas}} \approx 1.24 \times 10^7 M_{\odot} h^{-1}$ for gas and $M_{\text{dark}} \approx 6.51 \times 10^7 M_{\odot} h^{-1}$ for dark matter.

Our new black hole feedback model introduces several new parameters, and we must determine their values. However, computational resources limit our abilities to search all of the available parameter space and we must fix a large fraction of the parameters in order to explore the model further. In total we vary six parameters in our model, giving us a total of 576 simulations. First, we explain the fixed parameters and the motivation for those values.

4.1 Fixed parameters

There are two fixed parameters that describe the coupling of the energy from the black hole (BH) feedback in our model: $\epsilon_{\text{f,slim}}$ and $\epsilon_{\text{f,quasar}}$. The former is for the slim disc mode (high accretion rates) and the latter is for the quasar mode (mid-range accretion rates). Both of these parameters could be independent, but to reduce computational costs we fix both values to $\epsilon_{\text{f,slim}} = \epsilon_{\text{f,quasar}} = 0.05$. Note that the coupling factor for the momentum-driven feedback is degenerate with the cold gas accretion efficiency, ϵ_{cold} . The feedback coupling sets the normalization of the BH–stellar mass relationship by lowering the cold gas fraction in the BH environment. Simultaneously, ϵ_{cold} determines how much of that gas may be used to grow the BH. Therefore, we chose $\epsilon_{\text{f,quasar}}$ and $\epsilon_{\text{f,slim}}$ to be low values since ϵ_{cold} must be less than unity (i.e. it is an efficiency). Using lower values of $\epsilon_{\text{f,slim}}$ and $\epsilon_{\text{f,quasar}}$ actually result in a much lower mass loading than $\sim 20L/c$ but we choose to express everything in this form to separate the numerics from the physics.

Next, the wind velocities $v_{\text{wind,quasar}}$ and $v_{\text{wind,slim}}$ must be fixed in order to determine the accretion fractions in both the quasar and slim disc feedback modes. Similarly to the coupling factors, we fix $v_{\text{wind}} = v_{\text{wind,quasar}} = v_{\text{wind,slim}}$ due to the lack of observations of wind

¹ Although there are attempts to model subgrid scale dynamical friction forces, see e.g. Tremmel et al. (2017).

² <https://caesar.readthedocs.io/>

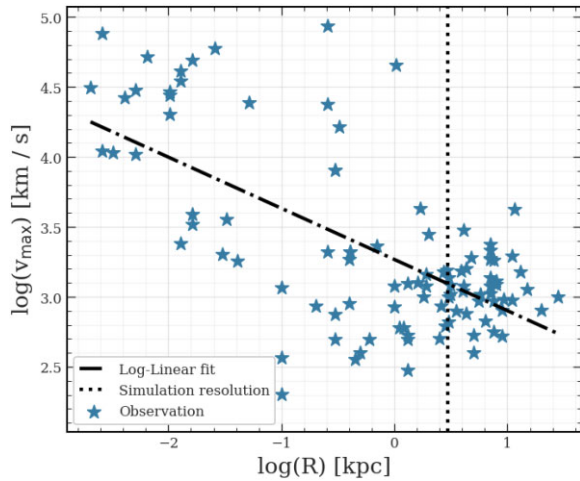


Figure 3. Active galactic nuclei wind velocities as a function of radius produced from Fiore et al. 2017. We fit a power law for illustrative purposes and found a relationship $\log(v_{\max}) = -0.366 \log(R) + 3.267$. For a typical cosmological simulation with resolution $\sim 2 \text{ kpc } h^{-1}$, wind velocities should be of the order of $\sim 1000 \text{ km s}^{-1}$.

speeds from rapidly accreting black holes. The observed physical wind velocities from quasar-like AGN range from $\sim 10^2 \text{ km s}^{-1}$ to $\sim 10^5 \text{ km s}^{-1}$ depending on the observed scale. We compiled wind maximum velocity results as a function of radius from Fiore et al. (2017) in Fig. 3. The dotted vertical line shows the simulation gravitational softening of $\sim 2 \text{ kpc } h^{-1}$. For illustrative purposes only, we show a log-linear fit to the observed data. Evidently, by the time winds launched from close to the black holes approach the scale of our simulation resolution, they should have already slowed down to $\sim 10^3 \text{ km s}^{-1}$. For that reason, we fix $v_{\text{wind}} = 10^3 \text{ km s}^{-1}$. Again, we must emphasize that the wind velocity is degenerate with ϵ_{cold} , and the feedback efficiency parameters. We attempt to use physically motivated values when possible to remove degeneracy.

The last two fixed parameters are the boundary accretion rate ratios separating the three modes: R_{lower} and R_{upper} . These accretion ratios determine when there is a break in the accretion efficiency, $\eta = \eta(j, \dot{M}_{\text{acc}})$. We follow Merloni & Heinz (2008) and set $R_{\text{lower}} = 0.03$ (see also Maccarone et al. 2003; Greene et al. 2006) so that below this value, $\eta \propto \dot{M}_{\text{acc}}/\dot{M}_{\text{Edd}}$. For the high accretion rate regime, we set $R_{\text{upper}} = 0.3$, as above this value the classical thin- α -disc model is suggested to break down (Laor & Netzer 1989; McClintock et al. 2006; Sądowski 2009; Madau et al. 2014).

4.2 Varied parameters

The six parameters that we choose to vary are: the jet loading, $\epsilon_{\text{f,ADAF}}$, $M_{\text{ADAF,limit}}$, v_{jet} , j , and whether the jet is isotropic or aligned with the angular momentum of the galaxy. All of the varied parameters (see Table 2), except for j , only impact the low accretion rate regime, i.e. $\dot{M}_{\text{acc}}/\dot{M}_{\text{Edd}} < R_{\text{lower}}$, in our calibration tests. As discussed in Section 2.1, j impacts the high accretion rate regime significantly through the accretion fraction f_{acc} . All of these parameters either do not have strong constraints or do not have a physical meaning, but only exist due to the insufficient resolution of our simulations.

4.3 Observational constraints and parameter choice

One of the more common methods for calibrating cosmological simulations is to compare some observational constraints at $z = 0$

Table 2. The six parameters that we vary for our calibration. The jet can either be energy or momentum conserving on the large scales. $\epsilon_{\text{f,ADAF}}$ is the coupling of the secondary feedback component in the ADAF mode. $M_{\text{ADAF,limit}}$ is the black hole mass at which the ADAF mode is allowed. v_{jet} is the jet velocity. j is the spin of all black holes. We also test the importance of the black hole jet direction by allowing it to be isotropic, or non-isotropic.

Parameter	Value 1	Value 2	Value 3	Value 4
Jet loading	Momentum	Energy	–	–
$\epsilon_{\text{f,ADAF}}$	0.001	0.01	0.1	–
$M_{\text{ADAF,limit}} (M_{\odot})$	0	3×10^7	7×10^7	10^8
$v_{\text{jet}} (\text{km s}^{-1})$	5000	7500	10^4	1.5×10^4
j	0.3	0.6	0.9	–
Isotropic Jet	Yes	No	–	–
$\epsilon_{\text{f,slim}}$	0.05	–	–	–
$\epsilon_{\text{f,quasar}}$	0.05	–	–	–
$v_{\text{wind,slim}}$	1000 km s^{-1}	–	–	–
$v_{\text{wind,quasar}}$	1000 km s^{-1}	–	–	–
R_{lower}	0.03	–	–	–
R_{upper}	0.3	–	–	–

to the simulated data, representing many variations of the free parameters, at the same redshift. Our choices in Sections 4.1 and 4.2 lead to 576 parameter variations that must be constrained. That is a significant number of simulations that would need to be run to $z = 0$ and so we tried an unconventional approach of calibrating our parameter variations to observations at $z = 2$ (corresponding to 33 per cent of the run-time, compared to $z = 0$) – allowing us to remove a large part of parameter space for parameter variations that have already failed by this time. We only ran the simulations that gave the best match to observations past $z = 2$, according to our criteria described below.

We choose three observational constraints³ for our parameter variations: (i) the galaxy stellar mass function (GSMF), (ii) the BH mass–stellar mass correlation, and (iii) the quenched galaxy density. While constraints (i) and (ii) are common, constraint (iii) is also necessary because SIMBA-like models (such as ours) will have difficulties producing sufficient quenched galaxies at high-redshift.

Our BH model is SIMBA-like insofar as we decided to use our radiative efficiency curve in a specific implementation of BH feedback. As previously discussed, our BH feedback model is truly the radiative efficiency curves in Fig. 1 and could be attached to any contemporary BH feedback implementation in Lagrangian or Eulerian based cosmological simulations. However, the kinetic jet and kinetic quasar wind in SIMBA (which uses a Lagrangian hydrodynamical solver) underpredicts high-redshift quenched galaxy densities (Merlin et al. 2019). That is in the nature of the model itself: the quasar mode does not have sufficient energy to quench galaxies, while the kinetic jet only activates after $z \sim 3$. The latter is either a *feature* of the model or a consequence of calibration. Regardless, we choose to calibrate our simulations to the quenched galaxy density at $z = 2$ in attempt to alleviate the issue.

Our $(25 \text{ cMpc } h^{-1})^3$ volumes are small and, therefore, may not contain a sufficient sample size to predict the correct quenched density. Therefore, we do not place a strong constraint on the quenched number density, but rather a minimum bound. The results of Merlin et al. (2019) (their fig. 7) suggest that there are somewhere

³See Schaye et al. (2015) for an excellent discussion of why galaxy stellar masses and black hole (BH) masses cannot be predicted in cosmological simulations.

between $\approx 10^{-4}$ to 5×10^{-4} quenched galaxies per cMpc^3 at $z = 2$. That gives approximately 5 to 15 quenched galaxies in our simulated volume. We are only really concerned about removing large parts of parameter space by stopping at $z = 2$, therefore we set the constraint that *there must be at least one*⁴ quenched galaxy in our volume to proceed the simulation to $z = 0$.

Constraints (i) and (ii) also do not require strict⁵ constraints since we are simply removing large sections of parameter space. For (i), we require the simulated GSMFs to have a galaxy number density $\gtrsim 10^{-4} \text{cMpc}^{-3}$ at $M_* \sim 3 \times 10^{11} M_\odot$, following the observations in Tomczak et al. (2014). For (ii), we produced the BH mass–stellar mass relationship by binning our simulated BH masses in bins of galaxy stellar masses (width $\Delta \log(M_*) = 0.2$) with the constraint that the galaxies are well-resolved, i.e. $M_* \gtrsim 10^{10} M_\odot$. We then found the mean value and standard deviation in each bin. We impose the constraint that the fit for the BH mass–stellar mass relationship in Kormendy & Ho (2013) must lay within one standard deviation of the simulated mean value curve to be acceptable. However, we found that using the accretion rate in equation (51) with a value of $\epsilon_{\text{cold}} = 0.06$ rarely leads to deviations from the Kormendy & Ho (2013) fit. Note that observations at $z = 2$ suggest that BHs may be above the Kormendy & Ho (2013) relationship. However, we know from experience with the SIMBA model that (a) BH feedback will be ineffective if the BHs are below the relationship, (b) BH feedback will be overeffective if the BHs are above the relationship, and, more importantly, (c) the normalization of the BH–stellar mass relationship is invariant in SIMBA-like models. Since it is invariant, if the BH masses are much greater than the Kormendy & Ho (2013) relationship at high redshift, they will remain above for all cosmic time and galaxies will be overquenched. Therefore, we must calibrate the relationship at $z = 2$, knowing they will stay on the relationship at $z = 0$.

Out of all of our 576 calibration simulations, only 56 satisfied all three of our constraints at $z = 2$. Interestingly, the quenched density was the dominant constraint that removed the bulk of parameter space, indicating that it is indeed difficult for SIMBA-like models to quench high-redshift galaxies. We show the parameters that gave us reasonable results in Table 3. It is immediately obvious that there seem to be no clearly favoured values for any of the parameters. These 56 runs span the possible values for $\epsilon_{f, \text{ADAF}}$, and have no preference for the loading type, or v_{jet} . However, there is a preference for $M_{\text{ADAF, limit}} > 0$, as well as lower values of $j \sim 0.3$. Additionally, there is a marginal preference for having an isotropic jet.

It is important to note that the quenched density constraint may be responsible for the limited number of successful runs not only because it is strict, but also due to the stochastic nature of the simulations themselves. Recall that we define quenched galaxies as those with $\text{sSFR} < 10^{-11} \text{yr}^{-1}$ and that there are few massive galaxies within the small volumes we simulated. When we evaluated the $\text{sSFR}-M_*$ relationship, we noticed that in some cases there were galaxies which were quite close to being quenched, but did not make the threshold. The inherent stochasticity combined with a firm constraint led to many calibration values being rejected. We again stress that the radiative efficiency model we present in this work does not necessarily have to be combined with a SIMBA-like model, and could be combined into any black hole feedback scheme, leading to a different calibration. We only discuss these 56 calibrations and their parameter values as a proof-of-concept.

⁴We simulated the same initial conditions with SIMBA, and found zero quenched galaxies at $z = 2$.

⁵Or, *hard* constraints in the language of constraint programming.

Not only are these calibrations able to reproduce the GSMF and the BH mass–stellar mass relationship but they are also able to broadly reproduce the observed cosmic star formation rate density (CSFRD) of the Universe down to $z = 0$, even though they were only calibrated to the three constraints at $z = 2$. While it is promising that the model calibrations reproduce a single unconstrained observable, we require verification in a larger volume to ensure better statistics and probe larger galaxy mass ranges, since the CSFRD is very sensitive to box size.

5 SIMULATED GALAXY POPULATION SURVEY

It is important to determine how well our new black hole (BH) feedback model can reproduce a realistic galaxy population. However, our calibration volume contained few galaxies on the mass scale where BH feedback is expected to be the most impactful – massive galaxies and galaxy groups/clusters. A much larger volume is necessary to probe these mass scales and, therefore, we decided to simulate a larger volume using a single parameter choice – our run labelled 165 (see Table 3). We chose this particular run since it had the lowest mean-squared error in the GSMF, compared to observations, at $z = 0$. Our simulation consists of one run with $N_{\text{gas}} = N_{\text{dark}} = 1024^3$ in a $(100 \text{cMpc } h^{-1})^3$ volume. The large-volume simulation uses exactly the same subgrid models and cosmology as described in Section 3, and have the same particle mass resolution as our calibration suite described at the beginning of Section 4.

5.1 Calibration constraints revisited

In Fig. 4 we show the simulated GSMF at six redshifts from our large $(100 \text{cMpc } h^{-1})^3$ volume. The redshifts are $z = 6, 4, 3$ in the left column from top to bottom, respectively, and then $z = 2, 1, 0$ from top to bottom in the right column, respectively. For redshifts $z \geq 4$, we compare with the observations in Song et al. (2016), whereas for $1 \leq z \leq 3$ we compare with both observational results from Muzzin et al. (2013) and Tomczak et al. (2014). For $z = 0$, we compare with both Baldry et al. (2012) and Bernardi et al. (2017). At each redshift we separate quenched (red) and star forming (blue) galaxies to show their contribution to the overall GSMF (shaded region). The overall GSMF includes a shaded region showing the impact of cosmic variance. At redshifts $z \geq 3$ the match to the GSMF is mostly due to star forming galaxies and is not due to the BH feedback model that we introduced. Rather, it is a result of the SIMBA cooling, star formation, and stellar feedback models providing a good fit to the observations. At redshifts $z \lesssim 4$, the BH feedback model begins to impact the quenched fraction within the volume, as is evidenced by the bottom left panels, where it is clear that massive galaxies are beginning to quench. By $z = 1$, the quenched population dominates the overall GSMF at the high-mass end, providing a reasonable match to the observations. However, at $z = 0$, our BH model provides a reasonable fit to the Bernardi et al. (2017) observations, where the entire contribution to the overall GSMF above $M_* \sim 10^{11} M_\odot$ is due to the quenched population. However, the model underpredicts the abundance of galaxies at the knee of the GSMF due to overquenching.

Fig. 5 shows the BH mass–stellar mass relation at $z = 0$ for our new model along with comparisons to ILLUSTRISTNG, EAGLE, FLAMINGO, and SIMBA. We include observational relations from Kormendy & Ho (2013) as well as Bentz & Manne-Nicholas (2018) as a comparison. Our model provides a reasonable fit for $M_* > 10^{10} M_\odot$ at $z = 0$, and effectively follows the results from the SIMBA simulation. This indicates that the simpler cold gas accretion model we use in this work is just as effective as the more complicated

Table 3. The six parameters that we vary for our calibration and their values for calibration simulations that were accepted under our constraints on the galaxy stellar mass function, black hole–stellar mass relation, and quenched density at $z = 2$.

Run label	$\epsilon_{f,ADAF}$	$M_{ADAF,limit} (M_{\odot})$	Loading type	v_{jet}	j	Isotropic jet
008	0.001	0	Energy	5000	0.3	No
041	0.001	5×10^7	Energy	5000	0.3	Yes
058	0.001	10^8	Energy	7500	0.3	No
059	0.001	10^8	Energy	7500	0.3	Yes
061	0.001	10^8	Energy	10 000	0.3	Yes
063	0.001	10^8	Energy	15 000	0.3	Yes
130	0.001	0	Momentum	7500	0.9	No
131	0.001	0	Momentum	7500	0.9	Yes
147	0.001	10^7	Momentum	7500	0.9	Yes
161	0.001	5×10^7	Momentum	5000	0.9	Yes
163	0.001	5×10^7	Momentum	7500	0.9	Yes
165	0.001	5×10^7	Momentum	10000	0.9	Yes
179	0.001	10^8	Momentum	7500	0.9	Yes
181	0.001	10^8	Momentum	10 000	0.9	Yes
183	0.001	10^8	Momentum	15 000	0.9	Yes
218	0.010	10^7	Energy	7500	0.3	No
222	0.010	10^7	Energy	15 000	0.3	No
223	0.010	10^7	Energy	15 000	0.3	Yes
224	0.010	5×10^7	Momentum	5000	0.3	No
232	0.010	5×10^7	Energy	5000	0.3	No
233	0.010	5×10^7	Energy	5000	0.3	Yes
235	0.010	5×10^7	Energy	7500	0.3	Yes
238	0.010	5×10^7	Energy	15 000	0.3	No
253	0.010	10^8	Energy	10 000	0.3	Yes
254	0.010	10^8	Energy	15 000	0.3	No
299	0.010	5×10^7	Energy	7500	0.6	Yes
313	0.010	10^8	Energy	5000	0.6	Yes
385	0.100	0	Momentum	5000	0.3	Yes
387	0.100	0	Momentum	7500	0.3	Yes
389	0.100	0	Momentum	10 000	0.3	Yes
391	0.100	0	Momentum	15 000	0.3	Yes
399	0.100	0	Energy	15 000	0.3	Yes
414	0.100	10^7	Energy	15 000	0.3	No
417	0.100	5×10^7	Momentum	5000	0.3	Yes
419	0.100	5×10^7	Momentum	7500	0.3	Yes
421	0.100	5×10^7	Momentum	10 000	0.3	Yes
423	0.100	5×10^7	Momentum	15 000	0.3	Yes
425	0.100	5×10^7	Energy	5000	0.3	Yes
429	0.100	5×10^7	Energy	10 000	0.3	Yes
432	0.100	10^8	Momentum	5000	0.3	No
434	0.100	10^8	Momentum	7500	0.3	No
436	0.100	10^8	Momentum	10 000	0.3	No
438	0.100	10^8	Momentum	15 000	0.3	No
442	0.100	10^8	Energy	7500	0.3	No
444	0.100	10^8	Energy	10 000	0.3	No
446	0.100	10^8	Energy	15 000	0.3	No
452	0.100	0	Momentum	10 000	0.6	No
472	0.100	10^7	Energy	5000	0.6	No
492	0.100	5×10^7	Energy	10 000	0.6	No
493	0.100	5×10^7	Energy	10 000	0.6	Yes
507	0.100	10^8	Energy	7500	0.6	Yes
510	0.100	10^8	Energy	15 000	0.6	No
569	0.100	10^8	Energy	5000	0.9	Yes
572	0.100	10^8	Energy	10 000	0.9	No
573	0.100	10^8	Energy	10 000	0.9	Yes
575	0.100	10^8	Energy	15 000	0.9	Yes

torque accretion model presented in Anglés-Alcázar et al. (2017) and used in the SIMBA simulations. The resolution of a galaxy in our simulation (~ 100 particles) is $\sim 3 \times 10^9 M_{\odot}$ and, therefore, the fit diverges at the low mass end. We emphasize that we calibrated to the relationship in Kormendy & Ho (2013) and only show the Bentz &

Manne-Nicholas (2018) relationship as it demonstrates the variety in observational results where other (e.g. EAGLE and FLAMINGO) simulations may provide a reasonable match to the slope.

Overall, the results of our calibration method used in this work are promising. The GSMF at $z = 0$ is in reasonable agreement

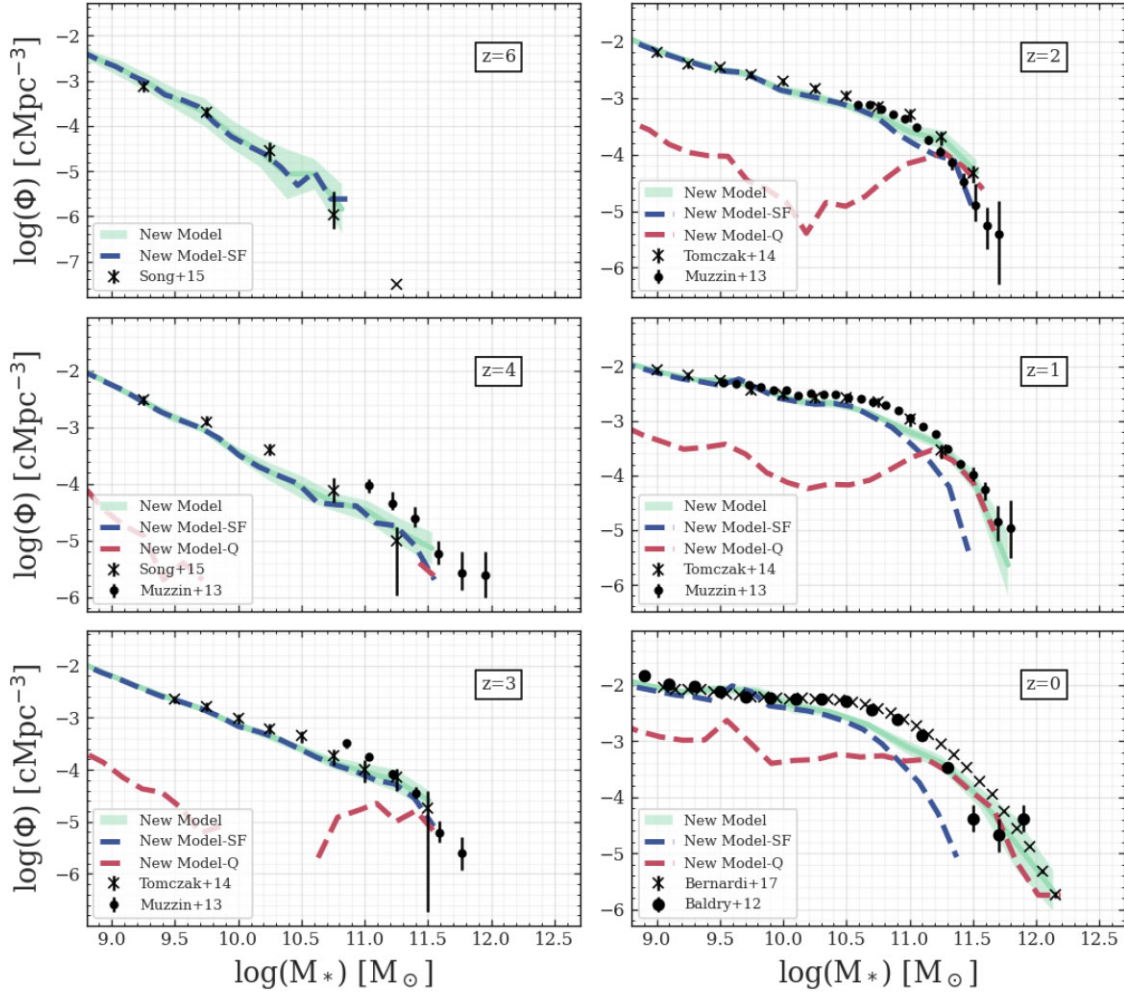


Figure 4. The observational and simulated galaxy stellar mass functions at $z = 6, 4, 3, 2, 1,$ and $z = 0$ from top-left to bottom-right, respectively. We use observations from Song et al. (2016) for $z = 6$ and $z = 4$, Muzzin et al. (2013) and Tomczak et al. (2014) for $z = 3, 2$ and $z = 1$, and Baldry et al. (2012) and Bernardi et al. (2017) for $z = 0$. We use calibration run 165 from Table 3 in a $(100 \text{ cMpc } h^{-1})^3$ volume, labelled as *New Model*, as a cyan shaded region (showing cosmic variance). We further divide the volume into both quenched and star forming galaxies at an sSFR cut of 10^{-11} yr^{-1} . The quenched galaxies are shown as a dark dashed line, and the star forming galaxies as a light dashed line. Our new model provides a reasonable match to the galaxy stellar mass function across all cosmic epochs, only underpredicting the knee of the galaxy stellar mass function by a factor of ~ 2 .

with observations, giving us confidence that our model is viable and that we can trust the stellar mass build-up in our simulated galaxy population. Similarly, our simulated BH–mass stellar mass relationship at $z = 0$ shows that our cold accretion model provides a reasonable growth rate with no divergences from the Kormendy & Ho (2013) relationship. The latter point is important and shows how, fundamentally, BH mass growing with the stellar mass build up could be more easily explained by the presence of cold gas in the cores of the galaxies.⁶

5.2 Star formation rates and efficiencies

The fundamental explanation for observed massive quenched galaxies in the Universe is that black hole (BH) feedback is sufficiently powerful to halt star formation in these systems – both by local injection of energy and by heating and lowering the density of gas in the halo, balancing cooling. In the previous section, we

demonstrate that our BH feedback model prevents the build up of stellar mass in galaxies – reproducing an exponential tail in the galaxy stellar mass function. In this section, we investigate the specific star formation rates (sSFRs) of our large-volume galaxy population in order to determine if the number of quenched systems matches the observations.

The top panel in Fig. 6 shows a 2D distribution of sSFRs (in Gyr^{-1}) and stellar masses, with the brightness of each bin indicating the log-normalized count of galaxies in that bin. The dash-dotted line shows the observationally motivated separation between quenched galaxies ($\text{sSFR} \lesssim 10^{-2} \text{ Gyr}^{-1}$) and star forming galaxies ($\text{sSFR} \gtrsim 10^{-2} \text{ Gyr}^{-1}$). The power-law overdensity of galaxies in the lower left section of the panel are galaxies with $\text{SFR} = 0 \text{ M}_{\odot} \text{ yr}^{-1}$. Our simulated galaxy population has a separate quenched population towards the lower right of this distribution (Bell et al. 2004). We do not include the observational results from SDSS here for clarity, but we now discuss the collapsed distribution of sSFRs.

The bottom panel in Fig. 6 shows the 1D sSFR distribution of our simulated sample (solid lines), showing the fraction of galaxies in each bin. We additionally divide the population into

⁶At least in these coarse grained models.

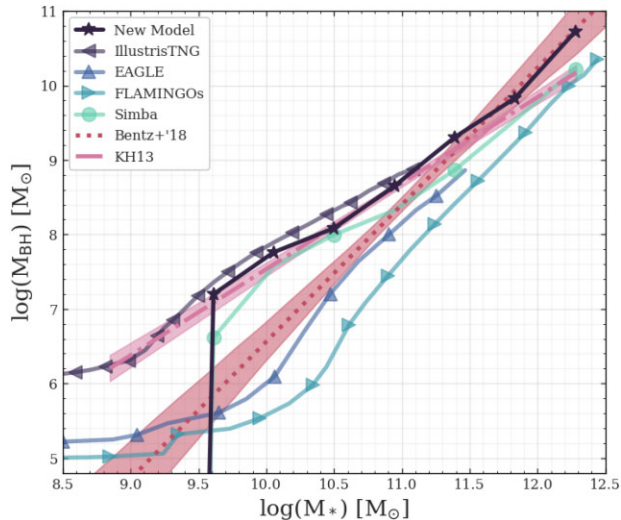


Figure 5. The black hole mass–stellar mass relationship. We show our new model in the $(100 \text{ cMpc } h^{-1})^3$ volume as a black solid line with star markers, in bins of M_* . We compare other large-volume simulations with markers given in the legend. The shaded regions show the Kormendy & Ho (2013) observed fit (KH13; dash-dotted) and the Bentz & Manne-Nicholas (2018) observed fit (dotted). In resolved galaxies ($M_* > 3 \times 10^9 M_\odot$), our new model matches the normalization and slope of the KH13 relationship.

three bins of stellar mass: (i) $10^9 < M_*/M_\odot < 10^{10}$ (blue), (ii) $10^{10} < M_*/M_\odot < 10^{11}$ (green), and (iii) $M_* > 10^{11} M_\odot$ (red). The dotted lines show the observational results from GALEX-SDSS-WISE catalogue, DR2 (Salim et al. 2016; Salim, Boquien & Lee 2018).

In our low mass galaxies, there is a slight shift in the location of the peak towards higher sSFR values and there are ~ 10 per cent quenched galaxies versus ~ 4 per cent expected from observations. In the middle mass range, effectively the knee of the GSMF, the distribution is peaked, but offset from the observations. The model underpredicts the fraction of quenched galaxies in this range by 20 per cent. In the high mass range, our model slightly overpredicts the number of star forming galaxies while providing a reasonable match to the number of quenched galaxies. The star forming massive galaxies have a broader distribution of observed sSFRs than our model.

In Fig. 7, we show the CSFRD history from our large-volume simulation. The dash-dotted line shows the observation compilation from Madau & Dickinson (2014). We do not show $z > 3$ since the CSFRD is modulated by the stellar feedback. While the approximate shape is predicted correctly, the normalization is a factor of $1.5\times$ below the peak. This again signals that the model is overquenching low-mass galaxies, and aligns with the GSMF.

In Fig. 8 we show the stellar mass–halo mass relationship (SMHM) for our simulated population, indicated by the line with a star symbol and error bars showing a standard deviation about the mean value in each bin of stellar mass. We show results from ILLUSTRISTNG (left triangle), EAGLE (upwards triangle), FLAMINGO (right triangle), and SIMBA (circle) for comparison. Instead of showing the observations directly, we show the abundance matching results from both Behroozi, Wechsler & Wu (2013) and Behroozi et al. (2019) for clarity. The shaded regions indicate their provided uncertainty bounds for their model calculations. Notice that in the updated abundance matching model, the high-mass end slope has become shallower. ILLUSTRISTNG, EAGLE,

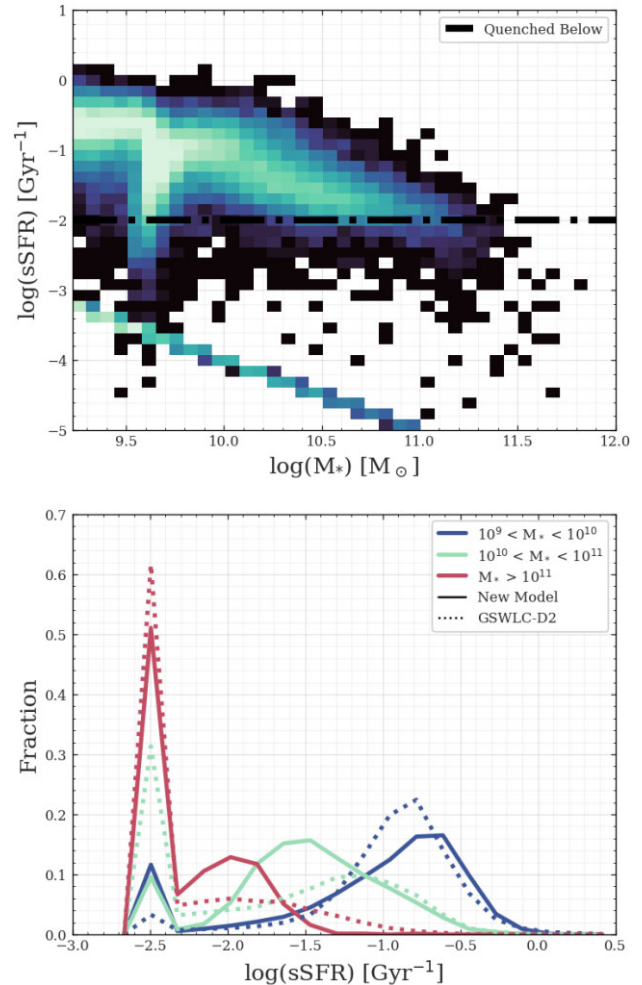


Figure 6. (top) A 2D histogram showing the log-normalized number of galaxies from our large-volume calibrated simulation, at $z = 0$, in bins of specific star formation rate (sSFR) and stellar mass (M_*). The dash-dotted line shows the upper limit in sSFR for considering a galaxy quenched. Our new model produces a star forming main sequence as well as a quenched distribution. (bottom) The 1D sSFR distribution from our calibrated large-volume simulation at $z = 0$, with each bin normalized to the total number of galaxies in the simulation. We divide the galaxies into three mass bins, as shown in the legend (solid curves). For comparison, we show observations from GSWLC-D2. Our new model overpredicts the number of quenched galaxies in the low-mass bin, as well as the high-mass bin.

and SIMBA provide the best predictions for the SMHM relationship, while FLAMINGO diverges from all other models above roughly $M_{\text{vir}} \gtrsim 10^{12} M_\odot$.

Our model provides a reasonable fit at masses $M_{\text{vir}} \gtrsim 10^{12} M_\odot$, but begins to diverge near $M_{\text{vir}} \lesssim 10^{12} M_\odot$. In particular, our model is successful at predicting a good estimate of the stellar efficiencies in the group and cluster regime, which we define as haloes in the mass range $M_{\text{vir}} \gtrsim 10^{13} M_\odot$. Unfortunately, our model underpredicts the stellar efficiencies in lower mass haloes compared to the updated Behroozi et al. (2019) model. The disagreement is only at a 0.25 dex level (less than a factor of approximately 2). In the group and cluster regime, our BH feedback model sufficiently prevents stellar mass build up across cosmic time that broadly agrees with the abundance matching predictions.

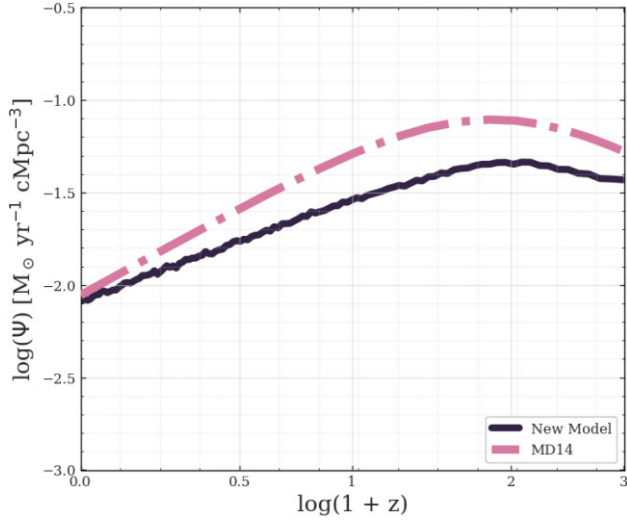


Figure 7. The star formation rate density history for our large-volume calibrated simulation from $z = 3$ to $z = 0$ (solid curve). The observational fit from Madau & Dickinson (2014) is shown as a dash-dotted curve (MD14). Our new model, although calibrated to completely different observables at $z = 0$ and $z = 2$ and in a much smaller volume, provides a reasonable prediction to the slope of the relationship from the peak at $z \approx 2$ to $z = 0$.

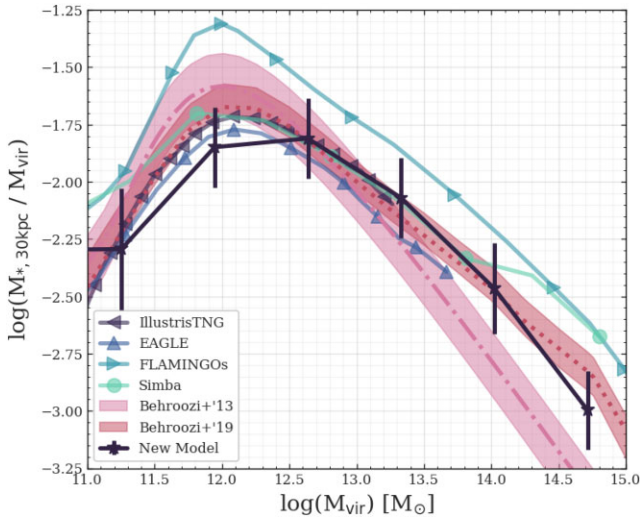


Figure 8. The stellar mass–halo mass relationship at $z = 0$, for central galaxies only. We show abundance matching results from Behroozi et al. (2013, 2019) as the shaded regions with dash-dotted and dotted lines, respectively. Our new model is the solid curve with star markers, and error bars given by the standard deviation of the value in each bin of M_{vir} . For comparison we show results taken from ILLUSTRISTNG, EAGLE, FLAMINGO, and SIMBA. Our model predicts a reasonable match to the abundance matching results, and especially succeeds at suppressing star formation in the brightest cluster galaxies at the galaxy-cluster scale.

5.3 Gas fractions

One important observational constraint for black hole (BH) feedback models is the total baryon fraction within galaxy groups and clusters. The universal ratio of baryons to total matter in the Universe depends on the cosmology as $f_{\text{baryon}} = \Omega_b / \Omega_m$, which for our selected cosmology (see Section 3) gives $f_{\text{baryon}} = 0.16$. Observationally, only the most massive haloes, i.e. galaxy clusters, retain this fraction within their virial radii (cf. fig. 8 in Liang et al. 2016), leading to

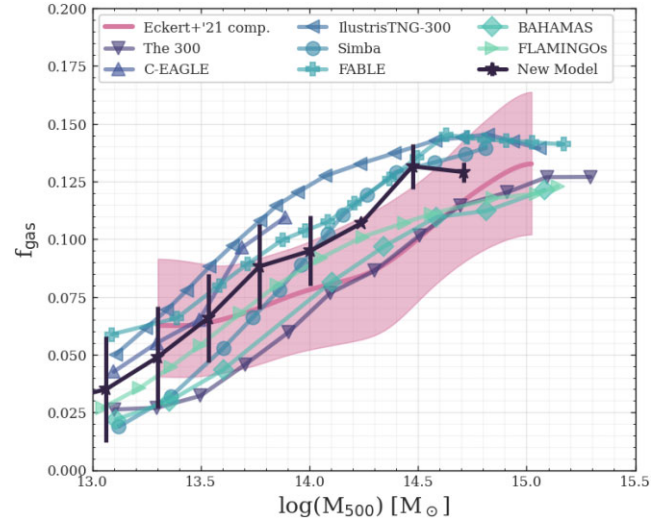


Figure 9. The hot gas fractions within galaxy groups and clusters. The shaded region with the solid pink line with no markers shows the observational compilation from the review in Eckert et al. (2021). We show our new model in black with star markers. For comparison, we show simulation results from THE 300, C-EAGLE, ILLUSTRISTNG-300, SIMBA, FABLE, BAHAMAS, and FLAMINGO, taken from fig. 15 in the review paper. Our new model tracks the ILLUSTRISTNG-300 model, while showing a promising trend towards the observed gas fractions in more massive clusters.

the idea that BH feedback is responsible for pushing gas outside of the virial radii of haloes with masses $M_{\text{vir}} \lesssim 10^{14} M_{\odot}$. The timing of gas ejection from the haloes is unclear in theoretical models as it is still an active area of research (see Eckert et al. 2021; Oppenheimer et al. 2021). It is important to note that the baryon fractions within the cores of haloes, i.e. $\lesssim R_{500}$, are difficult to constrain as they rely on assumptions of hydrostatic equilibrium and occasionally extrapolation since it is always not possible to measure out to R_{500} . Despite these difficulties, it is clear that there is a lack of baryons within the cores of galaxy groups and low-mass clusters, and any successful BH feedback model should be able to reproduce this trend.

Fig. 9 shows the hot gas ($T > 3 \times 10^5 \text{K}$) fractions $M_{\text{gas}}/M_{\text{total}}$ within R_{500} of the centre of each halo. Our model is the solid line with stars. We show simulation results from the 300 collaboration (downward triangle), C-EAGLE (upward triangle), ILLUSTRISTNG-300 (left triangle), SIMBA (circle), FABLE (plus sign), BAHAMAS (diamond), and FLAMINGO (right triangle) for comparison. Eckert et al. (2021) compiled observations into a single trend line with error, which we show as a solid line and shaded region, respectively.

Our new model produces gas fractions in line with those observed at the low-mass end of the group scale, jumping up at $M_{500} \sim 3 \times 10^{13} M_{\odot}$. At higher masses, up into the cluster scale, the gas fractions match the predictions from FABLE. Note that we did not calibrate to this relationship, did not test this mass scale, or investigate this redshift in our calibration simulations – it is a prediction of our model. Interestingly, our gas fractions remain above the observations while our stellar efficiencies (i.e. M_*/M_{vir}) remain low. That is counterintuitive to most of the BH feedback models available, as decreasing the gas fraction is paramount to effectively quenching the central brightest cluster galaxy. As an example, FLAMINGO was calibrated to the gas fractions in Fig. 9, but overall has much higher stellar efficiencies than any other simulation. That indicates that

perhaps our model is able to allow more control over the gas fractions while still being able to provide a quenched galaxy population.

Overall, the majority of simulations predict a slope that is too steep at all masses – indicating that the BH feedback models predict all galaxy groups and clusters have effectively a similar baryon fraction, counter to the observations. Notable exceptions are the 300 collaboration, C-EAGLE, and BAHAMAS simulations, which provide reasonable predictions for the normalization and the slope of the relationship. A full investigation into the impact of the model on the group and cluster scale is beyond the scope of this study, but we will investigate group and cluster baryon fractions in much more detail in a follow-up study.

6 CONCLUSIONS

The exponential decline in the observed number density of galaxies at high stellar masses suggests that powerful black hole (BH) feedback is a necessary component in our theoretical understanding of galaxy evolution. Models of BH feedback in cosmological simulations generally rely heavily on modelling feedback via radiation powered by accretion onto the BH, $E_{\text{feedback}} = \eta \dot{M}_{\text{acc}} c^2$. Typically, studies assume a quasar-like mode with a constant, spin-independent radiative efficiency $\eta \sim 0.1$, occasionally combined with a more powerful jet-like mode at low accretion rates to quench massive galaxies. We introduce the OBSIDIAN subgrid BH model: a model for large-scale cosmological simulations motivated by small-scale calculations of individual accretion flows that combines three physical regimes dependent on the accretion rate onto the BH, $\eta = \eta(j, \dot{M}_{\text{acc}})$. We divided the three regimes into the low accretion rate regime $\dot{M}_{\text{acc}}/\dot{M}_{\text{Edd}} \lesssim 0.03$, middle regime $0.03 \lesssim \dot{M}_{\text{acc}}/\dot{M}_{\text{Edd}} \lesssim 0.3$, and high regime $\dot{M}_{\text{acc}}/\dot{M}_{\text{Edd}} \gtrsim 0.3$ following an approach similar to the semi-analytic work of Merloni & Heinz (2008).

In the low accretion rate regime, we model BH accretion and feedback as an ADAF combined with a large-scale jet. In an ADAF, gas densities are low, such that much of the energy advects into the BH before it can radiate, leading to a low radiative efficiency. On the scales of cosmological simulations (\sim kpc) this model allows for two simultaneous feedback components: an isotropic outflow term combined with a collimated jet. The isotropic outflow term has a radiative efficiency that scales with the accretion rate as $\eta(j, \dot{M}_{\text{acc}}) \propto \dot{M}_{\text{acc}}/\dot{M}_{\text{Edd}}$ with the normalization set by continuity across the entire $\dot{M}_{\text{acc}}/\dot{M}_{\text{Edd}}$ range for η . We model the jet component following the calculations in Benson & Babul (2009) as a disc wind+jet, with disc wind efficiency taken from their fig. 3. We follow Talbot et al. (2021) and Huško et al. (2022) and implement a Blandford-Znajek (Blandford & Znajek 1977) jet.

For the middle accretion rate regime, or the quasar mode, we use a constant radiative efficiency $\eta = \eta(j)$ motivated by a model of a geometrically thin accretion disc. The normalization of η in this case comes from the simulations in Sądowski (2009), allowing us to set the normalization in the low accretion rate regime as well.

In the high accretion rate regime, we adopt the optically thick, geometrically slim disc model. At these accretion rates, energy dissipated in the disc is moved radially inwards faster than it can radiate, leading to a lower radiative efficiency with increasing \dot{M}_{acc} . We used the radiative efficiency fits from the simulations of Sądowski (2009) that lead to a behaviour $\eta(j, \dot{M}_{\text{acc}}) \propto (\dot{M}_{\text{acc}}/\dot{M}_{\text{Edd}})^{-1}$.

While the radiative efficiency function we provide in Section 2 could be applied to any implementation of BH feedback in cosmological simulations, we choose to incorporate it in the SIMBA galaxy formation model. SIMBA provides models for cooling, star formation, and stellar feedback over which we could test the impact of BH

feedback on the galaxy population. We inherit the BH seeding and repositioning algorithm from SIMBA, but made a slight alteration to the accretion rate estimator. While SIMBA uses the torque accretion mode from Hopkins & Quataert (2011) and Anglés-Alcázar et al. (2017), we introduce a cold accretion rate that scales with the cold gas mass near the BH as $\dot{M}_{\text{inflow}} \propto M_{\text{cold}}/t_{\text{ff}}$, where t_{ff} is the free-fall time estimated at the maximum influence radius of the BH. We found a proportionality constant of $\epsilon_{\text{cold}} = 0.06$ reproduced the behaviour of the more complicated torque accretion model, although it is degenerate with the quasar mode feedback normalization.

Using our modified SIMBA model as a base, we run a calibration suite of 576 cosmological simulations that varied six of our model parameters including the directionality of the jet, i.e. either isotropic or collimated, and whether it was energy or momentum loaded. We use observations and physically motivated arguments to fix the other six parameters of our model. Our 576 cosmological simulations consisted of volumes $(25 \text{ cMpc } h^{-1})^3$ with particle mass resolutions of $M_{\text{gas}} \approx 1.24 \times 10^7 M_{\odot} h^{-1}$ and $M_{\text{dark}} \approx 6.51 \times 10^7 M_{\odot} h^{-1}$ which were sufficiently large to contain a few galaxy-group scale objects. To constrain our parameters, we used the galaxy stellar mass function (Tomczak et al. 2014), BH mass–stellar mass relationship (Kormendy & Ho 2013), and the quenched number density of galaxies (Merlin et al. 2019) – all at a redshift of $z = 2$.

Out of the hundreds of calibration simulations, only 56 were viable to continue to $z = 0$. The main constraint that removes a significant portion of parameter space was the quenched galaxy number density as it seems difficult to quench galaxies at higher redshift in our model as implemented into a SIMBA-like framework. Given the low number of viable solutions, we use the calibration that had the lowest mean squared error compared to the observed galaxy stellar mass function at $z = 0$ and $z = 2$ as our fiducial model, but in a significantly larger volume.

We simulate a $(150 \text{ cMpc})^3$ volume to $z = 0$ with our fiducial model with 1024^3 gas and 1024^3 dark matter particles, which gave the same resolution as our calibration tests. In this volume, we investigate the galaxy stellar mass function, BH mass–stellar mass relation, specific star formation rate distribution, stellar mass–halo mass relation, and the baryon fractions within R_{500} of galaxy group-scale objects.

First, we analyse our three calibration constraints. The galaxy stellar mass functions across all redshifts provide reasonable fits. The BH mass–stellar mass relationship also matched the results from Kormendy & Ho (2013). Our model unfortunately predicts too many quenched lower mass galaxies ($M_* \lesssim 10^{11} M_{\odot}$), but provides a good estimation of the number of quenched, massive galaxies ($M_* \gtrsim 10^{11} M_{\odot}$).

Secondly, we analyse how well our model extrapolates to unconstrained observables: the stellar mass–halo mass function and the baryon fraction within galaxy groups and clusters.

Our model predicts a slightly lower normalization in the stellar mass–halo mass relation at masses $M_{\text{vir}} \lesssim 3 \times 10^{12} M_{\odot}$ but overall matches the normalization and slope of the abundance matching results from Behroozi et al. (2019). The peak of the relationship matched well, as well as the efficiencies at the galaxy cluster scale. These slight differences could be calibrated out of the model, by using the stellar mass–halo mass relationship as an additional constraint, if required.

The hot gas fraction within R_{500} is a useful observational constraint for BH feedback models as this is the region most impacted from the powerful outflows. In Fig. 9, we showed the hot gas fraction f_{gas} as a function of M_{500} for group to cluster scale haloes ($M_{500} \gtrsim 10^{13} M_{\odot}$) haloes in our large-volume simulation. We found that our model

provides a reasonable match to the observations in Eckert et al. (2021). Interestingly, our model provides a reasonably quenched galaxy population with haloes that have higher than observed gas fractions. That implies that gas is not being effectively removed from the halo and that the energy from the BH is injected more locally.

Overall, the OBSIDIAN subgrid model generates a suitable galaxy population for study. The main drawback is the overabundance of quenched, lower mass galaxies ($M_* \lesssim 3 \times 10^{10} M_\odot$). While we explore a wide range of possible parameters in this work, it is indeed possible that we have not found the set of parameters that best represents the galaxies across all mass scales. In this work, we focused heavily on the ADAF mode since it contains most of the new features when compared with SIMBA but computational resources limits how many parameters may be varied at once. One important step forward would be to design a parameter study for all parameters related to the slim disc and quasar modes, since those modes should most impact the lower mass galaxies. We additionally encourage further development of the model by adding a self-consistent spin distribution for the BHs, which could open up many research avenues into the impact of BHs on their galactic environs.

ACKNOWLEDGEMENTS

This research was enabled in part by support provided by the Digital Research Alliance of Canada. The majority of the simulations in this research were made possible by SciNet and the Niagara supercomputing cluster. DR and AB acknowledges the support of the Natural Sciences and Engineering Research Council of Canada (NSERC; funding reference number 534263) and through the Discovery Grant program. DR is supported by the Simons Foundation. AB acknowledges support from the Infosys Foundation via an endowed Infosys Visiting Chair Professorship at the Indian Institute of Science. Some of the simulations presented in this work were run on the Flatiron Institute’s research computing facilities (the Iron compute cluster), supported by the Simons Foundation. The authors thank Daniel Anglés-Alcázar, Sophie Koudmani, Fred Jennings, Alessandro Lupi, Christopher C. Hayward, Megan Tillman, and Asya Rennehan for useful advice during the course of this research. Additionally, we thank Dominique Eckert, and Annalisa Pillepich for providing observational and simulation data used for comparison in this work. Finally, we thank the anonymous referee for helping us to improve this work.

Our analysis was performed using the Python programming language. The following packages were used throughout the analysis: H5PY (Collette 2013), NUMPY (Harris et al. 2020), SCIPY (Virtanen et al. 2020), YT (Turk et al. 2011), and MATPLOTLIB (Hunter 2007). Prototyping of the analysis scripts was performed in the IPython environment (Perez & Granger 2007).

DATA AVAILABILITY

The data underlying this article will be shared on reasonable request to the corresponding author. We encourage further community development of the model, and will provide the source code on request.

REFERENCES

- Abramowicz M. A., Czerny B., Lasota J. P., Szuszkiewicz E., 1988, *ApJ*, 332, 646
- Anglés-Alcázar D., Davé R., Faucher-Giguère C.-A., Özel F., Hopkins P. F., 2017, *MNRAS*, 2853, 13
- Anglés-Alcázar D. et al., 2021, *ApJ*, 917, 53
- Babul A., White S. D. M., 1991, *MNRAS*, 253, 31P
- Babul A., Sharma P., Reynolds C. S., 2013, *ApJ*, 768, 11
- Baldry I. K. et al., 2012, *MNRAS*, 421, 621
- Bardeen J. M., 1970, *Nature*, 226, 64
- Bardeen J. M., Petterson J. A., 1975, *ApJ*, 195, L65
- Barnes D. J. et al., 2017, *MNRAS*, 471, 1088
- Beckmann R. S. et al., 2019, *A&A*, 631, 1
- Beckmann R. S., Dubois Y., Pellissier A., Polles F. L., Olivares V., 2022, *A&A*, 666, A71
- Behroozi P. S., Wechsler R. H., Wu H.-Y., 2013, *ApJ*, 762, 109
- Behroozi P., Wechsler R. H., Hearin A. P., Conroy C., 2019, *MNRAS*, 488, 3143
- Bell E. F. et al., 2004, *ApJ*, 608, 752
- Benson A. J., Babul A., 2009, *MNRAS*, 397, 1302
- Bentz M. C., Manne-Nicholas E., 2018, *ApJ*, 864, 146
- Bernardi M., Meert A., Sheth R. K., Fischer J.-L., Huertas-Company M., Maraston C., Shankar F., Vikram V., 2017, *MNRAS*, 467, stx176
- Berti E., Volonteri M., 2008, *ApJ*, 684, 822
- Blandford R. D., Znajek R. L., 1977, *MNRAS*, 179, 433
- Blanton E. L., Randall S. W., Clarke T. E., Sarazin C. L., Mcnamara B. R., Douglass E. M., McDonald M., 2011, *ApJ*, 737, 99
- Boehringer H., Voges W., Fabian A. C., Edge A. C., Neumann D. M., 1993, *MNRAS*, 264, L25
- Booth C. M., Schaye J., 2009, *MNRAS*, 398, 53
- Bourne M. A., Sijacki D., 2021, *MNRAS*, 506, 488
- Bourne M. A., Yang H.-Y. K., 2023, *Galaxies*, 11, 73
- Brienza M. et al., 2023, *A&A*, 672, A179
- Cattaneo A. et al., 2009, *Nature*, 460, 213
- Cenci E., Sala L., Lupi A., Capelo P. R., Dotti M., 2020, *MNRAS*, 500, 3719
- Chavan K., Dabhade P., Saikia D. J., 2023, *MNRAS*, 525, L87
- Choi E., Ostriker J. P., Naab T., Johansson P. H., 2012, *ApJ*, 754, 125
- Choi E., Ostriker J. P., Naab T., Oser L., Moster B. P., 2015, *MNRAS*, 449, 4105
- Choi E., Ostriker J. P., Naab T., Somerville R. S., Hirschmann M., Núñez A., Hu C.-Y., Oser L., 2017, *ApJ*, 844, 31
- Cielo S., Babul A., Antonuccio-Delogu V., Silk J., Volonteri M., 2018, *A&A*, 617, A58
- Ciotti L., Ostriker J. P., Proga D., 2009, *ApJ*, 699, 89
- Collette A., 2013, Python and HDF5. O’Reilly, Sebastopol, California
- Conroy C., Ostriker J. P., 2008, *ApJ*, 681, 151
- Crain R. A., van de Voort F., 2023, *ARA&A*, 61, 473
- Cui W. et al., 2022, *MNRAS*, 514, 977
- Czerny B., 2019, *Universe*, 5, 131
- Dalla Vecchia C., Schaye J., 2012, *MNRAS*, 426, 140
- Davé R., Anglés-Alcázar D., Narayanan D., Li Q., Rafieferantsoa M. H., Appleby S., 2019, *MNRAS*, 486, 2827
- Di Matteo T., Springel V., Hernquist L., 2005, *Nature*, 433, 604
- Di Matteo T., Colberg J., Springel V., Hernquist L., Sijacki D., 2008, *ApJ*, 676, 33
- Ding X. et al., 2020, *ApJ*, 888, 37
- Dubois Y., Devriendt J., Slyz A., Teyssier R., 2012, *MNRAS*, 420, 2662
- Dubois Y. et al., 2014, *MNRAS*, 444, 1453
- Dubois Y. et al., 2021, *A&A*, 651, A109
- Eckert D., Gaspari M., Gastaldello F., Le Brun A. M. C., O’Sullivan E., 2021, *Universe*, 7, 142
- Ellison S. L., Teimoorinia H., Rosario D. J., Mendel J. T., 2016, *MNRAS*, 458, L34
- Ellison S. L. et al., 2021, *MNRAS*, 505, L46
- Esin A. A., McClintock J. E., Narayan R., 1997, *ApJ*, 489, 865
- Faucher-Giguère C. A., Quataert E., 2012, *MNRAS*, 425, 605
- Fiacconi D., Sijacki D., Pringle J. E., 2018, *MNRAS*, 477, 3807
- Fiore F. et al., 2017, *A&A*, 601, A143
- Gaburov E., Nitadori K., 2011, *MNRAS*, 414, 129
- Gammie C. F., 1999, *ApJ*, 522, L57
- Gammie C. F., Shapiro S. L., McKinney J. C., 2004, *ApJ*, 602, 312
- Gofford J., Reeves J. N., Tombesi F., Braitto V., Turner T. J., Miller L., Cappi M., 2013, *MNRAS*, 430, 60

- Greene J. E., Ho L. C., Ulvestad J. S., 2006, *ApJ*, 636, 56
- Harris C. R. et al., 2020, *Nature*, 585, 357
- Henden N. A., Puchwein E., Shen S., Sijacki D., 2018, *MNRAS*, 479, 5385
- Hopkins P. F., 2015, *MNRAS*, 450, 53
- Hopkins P. F., Quataert E., 2011, *MNRAS*, 415, 1027
- Hopkins P. F., Kereš D., Oñorbe J., Faucher-Giguère C.-A., Quataert E., Murray N., Bullock J. S., 2014, *MNRAS*, 445, 581
- Hopkins P. F. et al., 2018, *MNRAS*, 480, 800
- Hopkins P. F. et al., 2023, *MNRAS*, 519, 3154
- Hopkins P. F. et al., 2024, *Open J. Astrophys.*, 7
- Hunter J. D., 2007, *Comput. Sci. Eng.*, 9, 90
- Huško F., Lacey C. G., Schaye J., Schaller M., Nobels F. S. J., 2022, *MNRAS*, 516, 3750
- Jamrozy M., Machalski J., Mack K.-H., Klein U., 2005, *A&A*, 433, 467
- Jetha N. N., Hardcastle M. J., Ponman T. J., Sakelliou I., 2008, *MNRAS*, 391, 1052
- Jung S. L. et al., 2022, *MNRAS*, 515, 22
- Kaviraj S. et al., 2017, *MNRAS*, 467, 4739
- King A., Pounds K., 2015, *ARA&A*, 53, 115
- Kormendy J., Ho L. C., 2013, *ARA&A*, 51, 511
- Koudmani S., Somerville R. S., Sijacki D., Bourne M. A., Jiang Y.-F., Profit K., 2024, *MNRAS*, 532, 60
- Kuźmicz A., Jamrozy M., Kozieł-Wierzbowska D., Weźgowiec M., 2017, *MNRAS*, 471, 3806
- Lacerda E. A. D., Sánchez S. F., Cid Fernandes R., López-Cobá C., Espinosa-Ponce C., Galbany L., 2020, *MNRAS*, 492, 3073
- Lammers C., Iyer K. G., Ibarra-Medel H., Pacifici C., Sánchez S. F., Tacchella S., Woo J., 2023, *ApJ*, 953, 26
- Lanson N., Vila J.-P., 2008a, *SIAM J. Numer. Anal.*, 46, 1912
- Lanson N., Vila J.-P., 2008b, *SIAM J. Numer. Anal.*, 46, 1935
- Laor A., Netzer H., 1989, *MNRAS*, 238, 897
- Liang L., Durier F., Babul A., Davé R., Oppenheimer B. D., Katz N., Fardal M., Quinn T., 2016, *MNRAS*, 456, 4266
- Lupi A., Haardt F., Dotti M., Fiacconi D., Mayer L., Madau P., 2016, *MNRAS*, 456, 2993
- Maccarone T. J., Gallo E., Fender R., 2003, *MNRAS*, 345, L19
- Machalski J., Chyży K. T., Stawarz Ł., Kozieł D., 2007, *A&A*, 462, 43
- Madau P., Dickinson M., 2014, *ARA&A*, 52, 415
- Madau P., Haardt F., Dotti M., 2014, *ApJ*, 784, L38
- McCarthy I. G., Babul A., Bower R. G., Balogh M. L., 2008, *MNRAS*, 386, 1309
- McCarthy I. G., Schaye J., Bird S., Le Brun A. M. C., 2017, *MNRAS*, 465, 2936
- McClintock J. E., Shafee R., Narayan R., Remillard R. A., Davis S. W., Li L., 2006, *ApJ*, 652, 518
- Merlin E. et al., 2019, *MNRAS*, 490, 3309
- Merloni A., Heinz S., 2008, *MNRAS*, 388, 1011
- Morganti R., 2017, *Front. Astron. Space Sci.*, 4, 1
- Murray N., Quataert E., Thompson T. A., 2005, *ApJ*, 618, 569
- Muzzin A. et al., 2013, *ApJ*, 777, 18
- Naab T., Ostriker J. P., 2017, *ARA&A*, 55, 59
- Narayan R., Igumenshchev I. V., Abramowicz M. A., 2003, *PASJ*, 55, L69
- Narayanan D. et al., 2021, *ApJS*, 252, 12
- Nemmen R. S., Bower R. G., Babul A., Storchi-Bergmann T., 2007, *MNRAS*, 377, 1652
- Nusser A., Silk J., Babul A., 2006, *MNRAS*, 373, 739
- O'Sullivan E. et al., 2012, *MNRAS*, 424, 2971
- Oppenheimer B. D., Babul A., Bahé Y., Butsky I. S., McCarthy I. G., 2021, *Universe*, 7, 209
- Perez F., Granger B. E., 2007, *Comput. Sci. Eng.*, 9, 21
- Pillepich A. et al., 2018, *MNRAS*, 475, 648
- Planck Collaboration XIII 2015, *A&A*, 594, A13
- Prasad D., Sharma P., Babul A., 2015, *ApJ*, 811, 108
- Prasad D., Sharma P., Babul A., 2018, *ApJ*, 863, 62
- Qiu Y., Bogdanović T., Li Y., Park K., Wise J. H., 2019, *ApJ*, 877, 47
- Reynolds C. S., McKernan B., Fabian A. C., Stone J. M., Vernaleo J. C., 2005, *MNRAS*, 357, 242
- Reynolds C. S., Brenneman L. W., Lohfink A. M., Trippe M. L., Miller J. M., Reis R. C., Nowak M. A., Fabian A. C., 2012, in Petre R., Mitsuda K., Angelini L., eds, *AIP Conf. Proc. Vol. 1427, Probing Relativistic Astrophysics around SMBHs: The Suzaku AGN Spin Survey*. Am. Inst. Phys., New York, p. 157
- Ricarte A., Narayan R., Curd B., 2023, *ApJ*, 954, L22
- Rosas-Guevara Y. M. et al., 2015, *MNRAS*, 454, 1038
- Ruszkowski M., Oh S. P., 2011, *MNRAS*, 414, 1493
- Sądowski A., 2009, *ApJS*, 183, 171
- Sądowski A., Narayan R., McKinney J. C., Tchekhovskoy A., 2014, *MNRAS*, 439, 503
- Sala L., Cenci E., Capelo P. R., Lupi A., Dotti M., 2020, *MNRAS*, 500, 4788
- Salim S. et al., 2016, *ApJS*, 227, 2
- Salim S., Boquien M., Lee J. C., 2018, *ApJ*, 859, 11
- Sanchez S. F. et al., 2018, *Rev. Mex. Astron. Astrofis.*, 54, 217
- Sazonov S. Y., Ostriker J. P., Ciotti L., Sunyaev R. A., 2005, *MNRAS*, 358, 168
- Schaye J. et al., 2015, *MNRAS*, 446, 521
- Schaye J. et al., 2023, *MNRAS*, 526, 4978
- Scheuer P., Feiler R., 1996, *MNRAS*, 282, 291
- Schutte Z., Reines A. E., Greene J. E., 2019, *ApJ*, 887, 245
- Shakura N. I., Sunyaev R. A., 1973, *A&A*, 24, 337
- Sijacki D., Springel V., Di Matteo T., Hernquist L., 2007, *MNRAS*, 380, 877
- Sijacki D., Vogelsberger M., Genel S., Springel V., Torrey P., Snyder G. F., Nelson D., Hernquist L., 2015, *MNRAS*, 452, 575
- Silk J., Rees M. J., 1998, *MNRAS*, 324, 128
- Smith K. L., Mushotzky R. F., Vogel S., Shimizu T. T., Miller N., 2016, *ApJ*, 832, 163
- Softan A., 1982, *MNRAS*, 200, 115
- Somerville R. S., Davé R., 2015, *Annu. Rev. Astron. Astrophys.*, 53, 51
- Song M. et al., 2016, *ApJ*, 825, 5
- Springel V., Di Matteo T., Hernquist L., 2005, *MNRAS*, 361, 776
- Su K.-Y. et al., 2021, *MNRAS*, 507, 175
- Talbot R. Y., Bourne M. A., Sijacki D., 2021, *MNRAS*, 504, 3619
- Talbot R. Y., Sijacki D., Bourne M. A., 2022, *MNRAS*, 514, 4535
- Talbot R. Y., Sijacki D., Bourne M. A., 2024, *MNRAS*, 528, 5432
- Tchekhovskoy A., McKinney J. C., Narayan R., 2012, *J. Phys.: Conf. Ser.*, 372, 012040
- Thorne K. S., 1974, *ApJ*, 191, 507
- Tombesi F., Cappi M., Reeves J. N., Palumbo G. G. C., Yaqoob T., Braitto V., Dadina M., 2010, *A&A*, 521, A57
- Tombesi F., Cappi M., Reeves J. N., Palumbo G. G. C., Braitto V., Dadina M., 2011, *ApJ*, 742, 44
- Tombesi F., Tazaki F., Mushotzky R. F., Ueda Y., Cappi M., Gofford J., Reeves J. N., Guainazzi M., 2014, *MNRAS*, 443, 2154
- Tomczak A. R. et al., 2014, *ApJ*, 783, 85
- Tremmel M., Karcher M., Governato F., Volonteri M., Quinn T. R., Pontzen A., Anderson L., Bellovary J., 2017, *MNRAS*, 470, 1121
- Turk M. J., Smith B. D., Oishi J. S., Skory S., Skillman S. W., Abel T., Norman M. L., 2011, *ApJS*, 192, 9
- Virtanen P. et al., 2020, *Nat. Methods*, 17, 261
- Vogelsberger M. et al., 2014, *MNRAS*, 444, 1518
- Weinberger R. et al., 2017, *MNRAS*, 465, 3291
- Weinberger R. et al., 2023, *MNRAS*, 523, 1104
- Wellons S. et al., 2023, *MNRAS*, 520, 5394
- Yuan F., Narayan R., 2014, *ARA&A*, 52, 529
- Zubovas K., King A., 2012, *ApJ*, 745, L34

This paper has been typeset from a $\text{\TeX}/\text{\LaTeX}$ file prepared by the author.